PNNL-35499

Feasibility Evaluation of a Solid Phase Scalable HEA Cladding Manufacturing Route

December 2023

Isabella J van Rooyen
Subhashish Meher
Jorge Dos Santos
Mageshwari Komarasamy
Mohan Nartu
Jonathan Wierschke
Ramprasad Prabhakaran
Nicole Overman
Irving Brown
Brian K Milligan
Lei Li
Ayoub Soulami
David Garcia
Tianhao Wang

M3FT-24PN060101052

Prepared for the U.S. Department of Energy
under Contract DE-AC05-76RL01830

DISCLAIMER

This report was prepared as an account of work sponsored by an agency of the United States Government. Neither the United States Government nor any agency thereof, nor Battelle Memorial Institute, nor any of their employees, makes **any warranty, express or implied, or assumes any legal liability or responsibility for the accuracy, completeness, or usefulness of any information, apparatus, product, or process disclosed, or represents that its use would not infringe privately owned rights**. Reference herein to any specific commercial product, process, or service by trade name, trademark, manufacturer, or otherwise does not necessarily constitute or imply its endorsement, recommendation, or favoring by the United States Government or any agency thereof, or Battelle Memorial Institute. The views and opinions of authors expressed herein do not necessarily state or reflect those of the United States Government or any agency thereof.

PACIFIC NORTHWEST NATIONAL LABORATORY
operated by
BATTELLE
for the
UNITED STATES DEPARTMENT OF ENERGY
under Contract DE-AC05-76RL01830

Printed in the United States of America

Available to DOE and DOE contractors from
the Office of Scientific and Technical Information,
P.O. Box 62, Oak Ridge, TN 37831-0062
www.osti.gov
ph: (865) 576-8401
fox: (865) 576-5728
email: reports@osti.gov

Available to the public from the National Technical Information Service
5301 Shawnee Rd., Alexandria, VA 22312
ph: (800) 553-NTIS (6847)
or (703) 605-6000
email: info@ntis.gov
Online ordering: http://www.ntis.gov

PNNL-35499

Feasibility Evaluation of a Solid Phase Scalable HEA Cladding Manufacturing Route

December 2023

Isabella J van Rooyen
Subhashish Meher
Jorge Dos Santos
Mageshwari Komarasamy
Mohan Nartu
Jonathan Wierschke
Ramprasad Prabhakaran
Nicole Overman
Irving Brown
Brian K Milligan
Lei Li
Ayoub Soulami
David Garcia
Tianhao Wang

Prepared for
the U.S. Department of Energy
under Contract DE-AC05-76RL01830

M3FT-24PN060101052

Pacific Northwest National Laboratory
Richland, Washington 99354

Summary

First of a kind development result on two low-energy solid-phase processes applied on an irradiation-resistant alloy, $NiCoFeCrCu_{0.12}$, are achieved and demonstrate moderate feasibility of successful tube fabrication using shear assisted processing and extrusion (ShAPE^{TM}) and friction stir layer deposition as a bulk manufacturing process.

The scope of the work is performed in four phases: 1) direct tube manufacturing of the irradiation-resistant high-entropy alloy (HEA) composite with increased strength, 2) co-shear lining manufacturing process for the increased strength and corrosion-resistant, irradiation-tolerant HEAs, 3) ShAPE of the radially gradient corrosion resistance alloy, and 4) alloy development and fabrication enabled through friction stir additive manufacturing processes among others.

This report describes the development activities from April to December 2023 to manufacture a direct customizable thin-walled tubular product from irradiation-tolerant composite high-entropy alloys (C-HEAs) while the overall project is continuing in 2024. This HEA tubular product is developed to exhibit enhanced high-temperature strength and compatibility in a variety of corrosive environments.

An approximately 2.5-inch hollow tube of Cu-HEA was produced on a first attempt and although significant process optimization and tooling modification are needed, the benefits of the ShAPE^{TM} extruded tube are demonstrated by:

- Grain refinement from an average grain size of 660 µm of the starting materials (as cast and homogenized materials) to produce grain size of 5–7 µm grain size structure after ShAPE processing. This method of extreme refinement of grain can enhance the grain boundary strengthening in HEAs. The mid-section of the tube seems to have marginally finer grains compared to that in both ends of the tube, which can be attributed to the more stable deformation conditions in that regen.
- The hardness in ShAPE processed Cu-HEA was also improved to an average HV value of 185 as compared to that of cast material (HV = 115). This enhancement of hardness is most probably due to grain boundary strengthening.
- As part of the corrosion mitigation design strategy, an invention was developed under a provisional patent, to form radially gradient material that can be used as an input material for the tube manufacturing ShAPE process.

Two four layered HEA structures were achieved after experiments to find a parameter space where stable plasticization was achieved.

> The interface regions showed finer grain structures with many dark particles which might be broken remnants from superficial oxide layers present on the previous deposition. This is possibly due to combined effects of thermo-mechanical stresses and heat affected zone due to a new top layer deposition. The extent of grain refinement in the friction surfacing layer deposition (FSLD) process appears to be smaller as compared to that in ShAPE process in the same alloy.

The hardness in FSLD processed Cu-HEA was found be to improve as compared to that in the as-cast samples mostly due to grain refinement in this solid-state processing. Furthermore, the hardness of the first layer of the FSLD processed Cu-HEA appears to be marginally higher (185 HV) than the other layers such as second layer (170 HV), third layer (170 HV), and fourth layer (172 HV) could also be attributed to the grain refinement.

Although the mechanical testing of the different layers is not yet completed, it showed a tensile strength of is ~590 MPa which is significantly higher that the base NiCoCrFe HEA (without Cu). However, at this point it needs to be determined if this increased strength is due to the deformation or due to the presence of Cu- rich nano precipitates in the FSLD processed Cu-HEA.

The very first ShAPE experiment was completed using an indirect extrusion setup in which the extrusion die enters the liner thereby leading to increased possibility of tooling failure. Due to the high strength properties of the HEA material, and the temperature rise during the experiment, significant tool damage occurred. Therefore, for the next set of experiments, a direct extrusion setup has been designed and is in the process of procurement. Furthermore, materials with increased temperature and force capability have been selected so that all the tooling sustains the extreme conditions experienced during extrusion of high temperature materials. The new set of tooling includes the following: 1) water-cooled die holder made from IN718, 2) extrusion dies made from W-Re-HfC since W-La_2O_3 extrusion die completely deformed during the first experiment, 3) a new larger chilled container assembly made from IN718, and 4) mandrels fabricated from W-La_2O_3 and W-Re-HfC. All these modifications were made to make sure the tooling survives the extrusion of the Cu-HEA.

Finally, the first attempts on both solid phase processes provided insight towards the next steps and deliver already first-of-a-kind result that shows promise to achieve the ultimate goals of this project to demonstrate feasibility of successful tube fabrication using ShAPE and friction stir layer deposition as a bulk manufacturing process. The project will continue to address challenges to increase the technology readiness levels.

Acknowledgments

The research presented here was supported by the Advanced Materials and Manufacturing Technology program of the U.S. Department of Energy (DOE) Office of Nuclear Energy. Pacific Northwest National Laboratory is operated for the DOE by Battelle under Contract No. DE-AC05-76RL01830. Our thanks to Dr. Zilong Hua and Dr, Robin Roper from Idaho National Laboratory for measuring the thermal diffusivity and differential scanning colorimetry analysis of the high-entropy alloy cast and homogenization material. Cary Counts is thanked for the technical editing of this report and Dr. Shivakant Shukla for the peer review of this report.

Acronyms and Abbreviations

AM	additive manufacturing
APR	advancing speed per revolution
BCC	body-centered cubic
DIC	differential interference contrast
dpa	displacement per atom
DSC	differential scanning colorimetry
EBSD	electron backscatter diffraction
EDS	energy dispersive spectroscopy
FCC	face centered cubic
FSAM	friction stir additive manufacturing
FSLD	friction surfacing layer deposition
HEA	high-entropy alloy
HIP	hot isostatic pressing
IPF	inverse pole figure
LFA	laser flash analysis
ODS	oxide-dispersion strengthened steel
PM	powder metallurgy
PNNL	Pacific Northwest National Laboratory
RPM	revolutions per minute
SEM	scanning electron microscopy
ShAPE^{TM}	shear assisted processing and extrusion
SPH	smoothed particle hydrodynamics
SPP	solid-phase processing
XRD	X-ray diffraction

Contents

Figures

Tables

1.0 Introduction

This report describes the development activities from April to December 2023 to manufacture a direct customizable thin-walled tubular product from irradiation-tolerant composite high-entropy alloys (C-HEAs) while the overall project is continuing in 2024. This HEA tubular product is developed to exhibit enhanced high-temperature strength and compatibility in a variety of corrosive environments. Additionally, a bulk solid phase additive manufacturing process, friction stir layer deposition (FSLD) has demonstrated unique grain refinement capabilities.

The initial scope of the project is focusing on the tube manufacturing process and property enhancement enabled by two low-energy SPP processes for a recently developed irradiation-resistant alloy, $NiCoFeCrCu_{0.12}$ [1]. This alloy contains a high density of Cu-rich nanoprecipitates distributed in the HEA matrix, showing excellent void swelling resistance and negligible radiation-induced hardening upon irradiation up to high radiation doses (i.e., higher than 100 displacement per atom [dpa]), which is significantly better than NiCoFeCr concentrated solid-solution alloys and austenitic stainless steels. Later stages of the continued project will expand into HEA alloy development as well. It is envisaged that new intellectual property may results from this research.

1.1 Scope

Tube fabrication processes for HEA alloys are still in early research and development phases because it is difficult to prevent segregation on the bulk scale. Furthermore, the presence of nanocomposites can further complicate the manufacturing processes because homogenous distribution of the nano features must be confirmed, and feature coarsening must be prevented during the manufacturing processes. To address this need, this work develops a first-of-its-kind multiple integrated deformation-based manufacturing process that could provide an economic pathway and the flexibility needed for adopting high-irradiation cladding applications.

The scope of the work is performed in four phases: 1) direct tube manufacturing of the irradiation-resistant HEA composite with increased strength, 2) co-shear lining manufacturing process for the increased strength and corrosion-resistant, irradiation-tolerant HEAs, 3) shear assisted processing and extrusion (ShAPE™) of the radially gradient corrosion resistance alloy, 4) alloy development and fabrication enabled through friction-stir additive manufacturing (FSAM) processes among others.

Low-energy-intensity solid-phase processing (SPP) approaches toward microstructure homogenization that will be deployed are shown in Figure 1. SPP and ShAPE are techniques that add an additional shear force compared to conventional extrusion approaches (Figure 2). Significant advantages of ShAPE are that it can be free from feedstock pre-consolidation and preheating, it is more energy-efficient, and it produces products with better strength, ductility, toughness, and surface finish [2]. In this research, more flexible feedstock manufacturing routes also are considered and investigated to enhance economic and product performance benefits. These flexible raw materials may include other additive manufacturing and SPP processes such as FSAM)/FS layer deposition (LD).

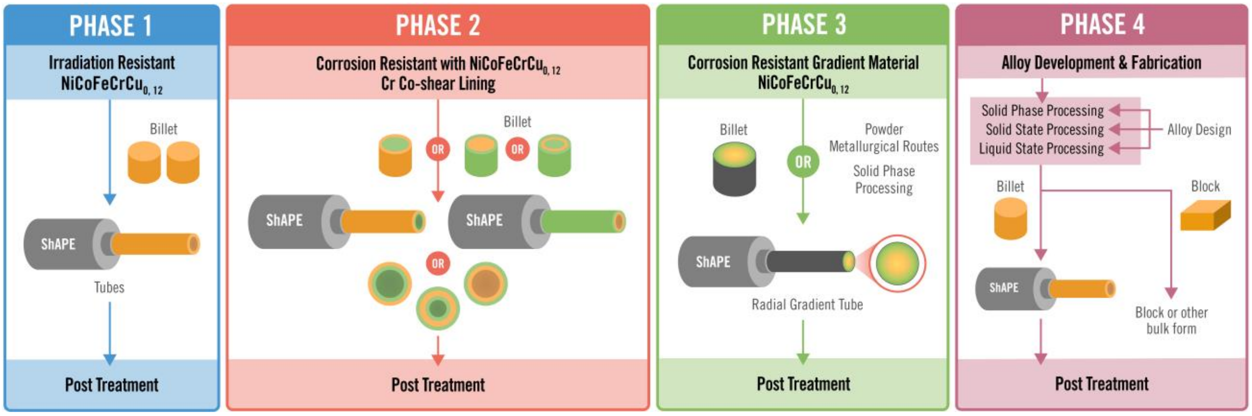

Figure 1. The scope of the work is performed in four phases: 1) direct tube manufacturing of the irradiation-resistant HEA composite with increased strength, 2) co-shear lining manufacturing process for the increased strength and corrosion-resistant, irradiation-tolerant HEAs, 3) ShAPE of the radially gradient corrosion resistance alloy, 4) Alloy development and fabrication.

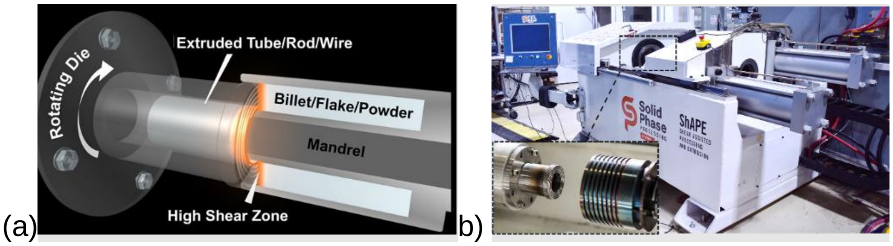

Figure 2. (a) The ShAPE process uses shear to locally heat, consolidate, and extrude materials. (b) The world's first dedicated ShAPE machine at Pacific Northwest National Laboratory (PNNL).

Coupled with tube functional design optimization, SPP is used to increase corrosion resistance through co-extruded multilayered bonded tubing and powder metallurgical processing gradient material as starting material for the ShAPE process. SPP, can therefore provide both an axial and radial gradient functional tube. SPP tube forming allows for continuous transition to a more economic material, reducing welded sections and simplifying welding of tubing to other components. The proposed work will co-extrude Cr with nanocomposite HEAs to provide corrosion protection. Based on the application, the Cr cladding can be applied either along the inside or outside of these tubes using the ShAPE process.

The current progress of activities performed from April 2023 to December 2023 are discussed to provide a conclusion on the feasibility of HEA tube fabrication enabled through AM techniques. Work performed under Phases 1, 3, and 4 are discussed, with only limited work to date performed for Phase 2. This included the initial Thermo-calc work performed to determine the possible interaction between the HEA alloy and Cr layers and reported in [3]. The ShAPE experimentation will continue after successful completion of the next HEA tube sample fabrication experiment scheduled once the new design tooling and die arrive.

1.2 Current State-of the-Art Technologies

1.2.1 Alloy Choice and Phase Diagram

Depending on alloy systems and compositions, precipitation of secondary intermetallic compound within the HEA matrix may be possible, further enhancing the mechanical strength and irradiation resistance. Keeping the strengthening ceramics and intermetallic phases at nanoscale will maximize the interfacial area density and toughen the composite. These AM techniques need to capitalize on the benefits of producing C-HEAs with controlled grain sizes and desired reinforcement distributions for enhanced creep resistance, irradiation resistance, and chemical stability of conventionally manufactured alloys. This potential for property enhancement exists for AM processing techniques that can develop materials with tailored microstructures ideal for enhanced physical and/or mechanical properties.

HEAs containing multiple principal elements are known to exhibit good mechanical properties, excellent corrosion, and oxidation resistance and are therefore suitable candidates for various structural applications [4-9]. Recent efforts have been focused on investigating the radiation response of certain HEAs for advanced nuclear energy applications [10]. The NiCrFeMn HEA exhibits a significantly lower void swelling and radiation-induced hardening and segregation at elevated temperatures (400–700℃) and 10 dpa compared to conventional FeNiCr-based alloys [11]. When Mn is replaced with Co, the HEA (NiCrFeCo) exhibits 10 times lower radiation-induced void swelling (at 53 dpa) than NiCo-based alloys [12,13]. However, it is argued that the single-phase HEAs, with reasonably simple microstructures like the abovementioned HEAs, reveal significant void swelling and fail to maintain their structural integrity when irradiated at >50 dpa [14-16]. Considering this, several HEAs with complex microstructures and high-density interfaces were investigated for operation under high radiation doses (>200 dpa). In a recent study by El-Atwani et al., the formation of Cr- and V-rich secondary precipitates within the body centered cubic matrix resulted in a remarkably lower radiation-induced hardening for the W-based HEA [16].

On the other hand, adding specific elements such as Cu, Al, and Ti also can enhance the radiation resistance of the NiCoCrFe face centered cubic (FCC)-HEA [30]. The addition of these elements is reported to induce second-phase precipitation in the NiCoCrFe-based HEAs [31-33]. Kombaiah et al. [1] doped the equiatomic NiCoCrFe HEA with three atom % of Cu and fabricated the $NiCoFeCrCu_{0.12}$ HEA using the floating-zone solidification method and subsequentially annealed the HEA to fabricate a microstructure with a high density of interphase boundaries arising from Cu-rich nanoprecipitates. The Cu precipitates act as sink sites for absorbing the point defects generated during irradiation, thereby enhancing the radiation resistance of the $NiCoFeCrCu_{0.12}$ HEA even at higher dosages. For instance, when irradiated with Au ions at 100, 350, and 500 dpa doses at 475 °C, void swelling of only < 0.01% was observed. The resistance to radiation-induced hardening and void swelling of the $NiCoFeCrCu_{0.12}$ HEA is remarkably higher than the NiCoCrFe HEA under ion irradiations up to a dose of 500 dpa for temperatures between 475–580°C. The void swelling resistance of this HEA is notably better than the austenitic stainless steels and comparable to the oxide dispersion-strengthened steels that are challenging and more expensive to fabricate. Therefore, the $NiCoFeCrCu_{0.12}$ HEA is chosen for investigation under the current work package.

1.2.2 Advantages for Using SPP Manufacturing for this Development

ShAPE^{TM} has been demonstrated for a variety of materials, including aluminum, magnesium, copper, metal matrix composites, steel, and oxide-dispersion strengthened (ODS) steel.

Research shows improved mechanical properties, fewer processing steps, and lower energy intensity through reduction or elimination of additional thermal processing [17]. Co-extrusion was successfully demonstrated [18] via the ShAPE process on various alloys systems. Ni-based alloys are widely used for high-temperature applications on account of their superior creep strength and oxidation resistance, although this poses a limitation for high neutron flux applications due to its neutron cross section. FeCrAl-based alloys are used but do not provide high-temperature strength in reactor applications either.

Tooling design and optimization are key parts during the execution stage. Although lessons learned from prior work will be utilized, material compatibility studies will be performed. The benefits of ShAPE™ for this project include the following: 1) low fabrication temperatures, eliminated melt-related defects such as porosity and cracking typically associated with casting or AM techniques, decreased segregation of elements, refined grains, and prevented dissolution or growth of precipitates, 2) the homogenous equiaxed grain microstructure, because of the recrystallization at high temperature 3) nanoprecipitates homogenously distributed and/or engineered for alignment and strength, irradiation behavior, and thermal conductivity, 4) design and formation of other non-reactive nanostructures for improved irradiation resistance, and 5) enhanced corrosion protection may not be fully achieved by compositional and homogenized microstructures due to competing requirements. Therefore, by implementing co-shear lining tube manufacturing processes and gradient tube processes, prior art on Ni-liners were demonstrated using Zircaloy.

1.2.3 Corrosion Behavior

Some research has been performed to study the corrosion characteristics of HEAs. One of the difficulties in fully characterizing their corrosion behavior is the wide variety of stoichiometries in the HEAs and the variety of corrosion environments. Thus, even though the literature exists, it may be difficult to determine how closely it applies to other materials and environments of interest. Overall, the literature seems to indicate that the corrosion behavior of HEAs is superior to many carbon steels and aluminum alloys.

Following are key points for the design and manufacturing approach to minimize corrosion:

Chromium is a key element in the corrosion resistance of stainless steels. As chromium concentration increases, the steels start to form a Cr oxide/hydroxide passivation layer on the surface. It is anticipated that Cr will display similar passivation effects in HEAs [19].

Nickel can be added to stainless steels to stabilize the austenite phase and improve corrosion resistance. However, there appears to be a limit to the amount of Ni that is beneficial to corrosion resistance. Beyond this limit, corrosion rates have been reported to increase.

Copper is primarily added to steels to improve mechanical properties despite its negative impact on corrosion resistance. The effect on corrosion is affected by the microstructure of the copper-containing phases. Copper-containing alloys form interdendritic phases that are preferentially dissolved.

A study of corrosion in FeCoNiCrCux HEAs (with $x = 0$, 0.5, and 1) showed that corrosion preferentially occurred at interdendritic phases [20].

Processing methods, including aging treatments, have also been carefully selected to achieve selected mechanical and even corrosion-resistant properties. The manufacturing of extruded HEAs using ShAPE will plausibly influence the corrosion behavior of these materials.

The corrosion of materials depends on more than just the chemistry of the material and the environment. The microstructure of the material can have a significant impact on oxidation [21], pitting [22], stress corrosion cracking [23], and diffusivity of species into the bulk material [24], among other electrochemical and mechanical effects. The manufacturing process that the material goes through will influence the final microstructure. The use of friction extrusion in manufacturing is no exception [25]. With the increased interest in the use of friction extrusion, it is important to understand just how this process affects the corrosion potential of the materials.

1.2.4 Modeling and Simulation

ShAPE is a complicated thermomechanical process that involves large material deformation, complex die/billet contact, and copious heat generation to maintain the processing temperature. Process modeling of ShAPE can help understand the associated physics, reveal the process parameter/condition relationship, and design for optimized tooling geometries and process parameters. The current knowledge provides a strong foundation for this work; however, it can be noted from Figure 3 that the HEA used in this research fell well outside the envelope of the materials previously manufactured and was the first attempt of a high strength material's tube fabrication via ShAPE. A previously developed smoothed particle hydrodynamics (SPH) modeling framework [26,27] used prior tube-forming material parameters to find an initial starting parameter window for new material types and was discussed in [3]. The SPH model accurately predicts material flow, stress-strain, temperature, strain rate, and grain size given certain process parameters for various AM techniques, such as ShAPE and friction extrusion of aluminum alloys, ShAPE™ of multi-alloy cladded tubing with dissimilar materials such as 1100/6061/7075 and Cu/Ni, friction stir welding/processing welding/processing (FSW/FSP) of aluminum alloys and stainless steels, and cold spray of Mg/Zn material systems. Prior experiences of producing bars through high-shear extrusion processes show that the SPP can be applied to materials that elastically deform and are thermally and chemically compatible with the tooling [26].

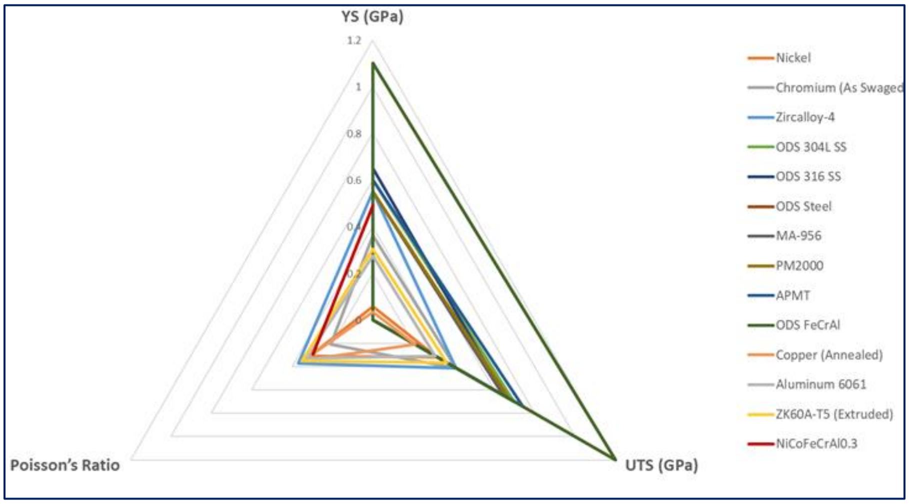

Figure 3. Property envelope of the materials previously considered for cladding or materials that have already been used by PNNL for tube and bar manufacturing via the ShAPE process.

1.2.5 Irradiation Behavior of the Material

Only limited irradiation behavior is available for the alloy used in this study, and as a baseline, a summary of the irradiation response of $Al_{0.3}CoCrFeNi$ HEA, which properties were used for the SPH modeling in interim, is also provided.

Al0.3CoCrFeNi irradiation conditions: 3MeV Au ions at temperatures ranging from 250°C to 650°C (~31 dpa)

No voids were observed in the $Al_{0.3}CoCrFeNi$ irradiated with 3 MeV Au ions at all four temperatures [28]. However, void swelling is observed in many other lower-mass ion-irradiated HEAs [29,30]. The void swelling response depends upon the type of the implanted ions and the irradiation energy. Therefore, irradiation experiments using higher energy and lower mass ions would be necessary to investigate the void swelling resistance of $Al_{0.3}CoCrFeNi$ HEA. The average size of the defect clusters increased while the defect density decreased with increased irradiation temperature of the single-phase $Al_{0.3}CoCrFeNi$ HEA. The evolution of irradiation-induced defects with temperature is identical to the conventional FCC alloys and is determined by the mobility and thermal stability of interstitials and vacancies.

Irradiation by 3 MeV Au ions also produces competing effects, such as irradiation-induced ballistic mixing and irradiation-enhanced diffusion, which affect the microstructural phase stability at different temperatures. For instance, ballistic mixing dominates at lower temperatures (≤500°C), thus suppressing $L1_2$ phase precipitation. In contrast, irradiation-enhanced diffusion dominates at elevated temperatures, resulting in the precipitation of the B2 phase. Irradiation-enhanced diffusion increases the atom mobility, and irradiation-induced dislocations serve as nucleation centers for the *B2* precipitates [28]. In another study, the nanoindentation results suggest that the irradiation-induced hardening at 500 °C was noticeably lower in the $Al_{0.3}CoCrFeNi$ HEA compared to 316H Stainless steel [31].

$CoCrFeNiCu_{0.12}$ Irradiation Conditions: 3 MeV Ni^{2+} at 500 °C (~106 dpa)

The void swelling of $CoCrFeNiCu_{0.12}$ HEA resulting from the irradiation at 500°C and ~106 dpa is less than 0.1% which is significantly lower than most single-phase FCC HEAs, FCC/back centered cubic steels, and ODS alloys [1]. The remarkable void swelling resistance is due to the presence of fine scale Cu-rich nano precipitates within the FCC matrix of this alloy. The density of radiation induced dislocations in this HEA is two orders of magnitude lower than the base NiCoCrFe HEA. Furthermore, this HEA also reveals no radiation induced hardening when irradiated at similar conditions. The average size of the Cu-rich nanoprecipitates increased, while the number density and the volume fraction of the precipitates decreased upon irradiation at 500°C and ~106 dpa. The results presented in [5] conclude that the effective point defects recombination at the (Cu- rich) precipitate/matrix interface enhances the radiation resistance in this HEA.

1.3 $NiCoFeCrCu_{0.12}$ HEA Baseline Material Properties

1.3.1 Phase Diagram

Cast rods of $NiCoFeCrCu_{0.12}$ HEA fabricated by vacuum induction melting were procured from sophisticated alloys for this study. The cast microstructures are typically non-homogeneous, so a homogenization solution treatment was implemented in the as-cast alloy, as described in Report M4FT-23PN060101061 [3]. The pseudo-binary diagram for this alloy is added again as it is used for clarification and discussion of the experimental conditions and choices were made in this study. The pseudo-binary phase diagram (NiFeCoCu$_{0.12}$ with Cr addition) was generated by Thermo-Calc^{TM} using the TCHEA3 database and is presented in Figure 4. The vertical dotted line (at 24.25% of Cr) represents the NiCoFeCrCu$_{0.12}$ HEA. It was evident that the solvus or the homogenization temperature for NiCoFeCrCu$_{0.12}$ HEA is ~1090 °C, as indicated by the dotted horizontal line on the phase diagram. Because there could be discrepancies in the predicted and experimentally observed temperatures, a temperature of 1200 °C and a duration of 6 h was chosen for homogenizing the as-cast microstructures of this HEA.

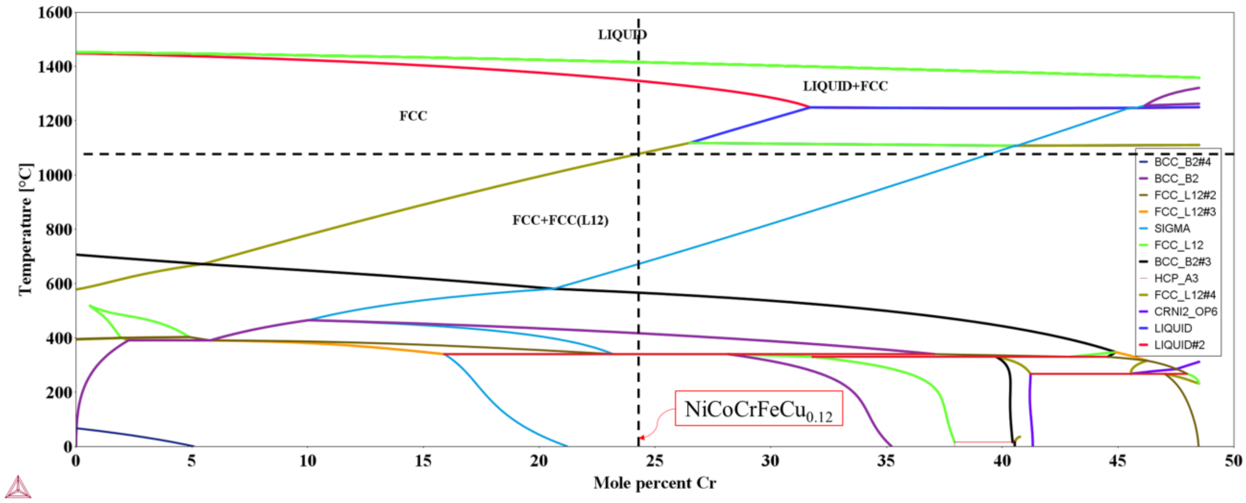

Figure 4. Pseudo-binary phase diagram generated using Thermo-Calc software

1.3.2 Microstructure, Grain Size and Hardness

The cast billet was characterized by a dendritic microstructure with elongated grains with striations. To homogenize the microstructure prior to solid phase processing, the billets were solution treated at 1,200°C for 6 hours. After homogenization, near equiaxed grains were formed with an average size of 660 mm. The average hardness value of the solutionized condition sample was 114.75 HV (Figure 5).

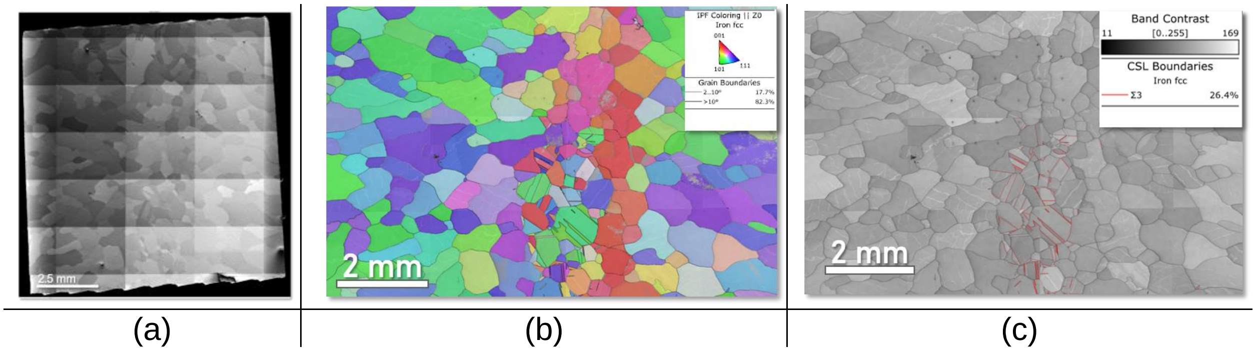

(a) (b) (c)

Figure 5. (a) Scanning electron microscopy (SEM) montage of the billet microstructure after solutionization; (b) and (c) microstructure of the solutionized material displaying near equiaxed grains.

Figure 6 shows the schematic of the experimental plan starting with the as-cast Cu-HEA and its homogenization treatment that served as the starting material for both ShAPE and FSLD experiments (details of the as cast and solution treated microstructures are provided in [3]). The ShAPE experiment microstructure characterization is shown in Section 2.6 and those after the Friction stir layer deposition in Section 4.3.2.

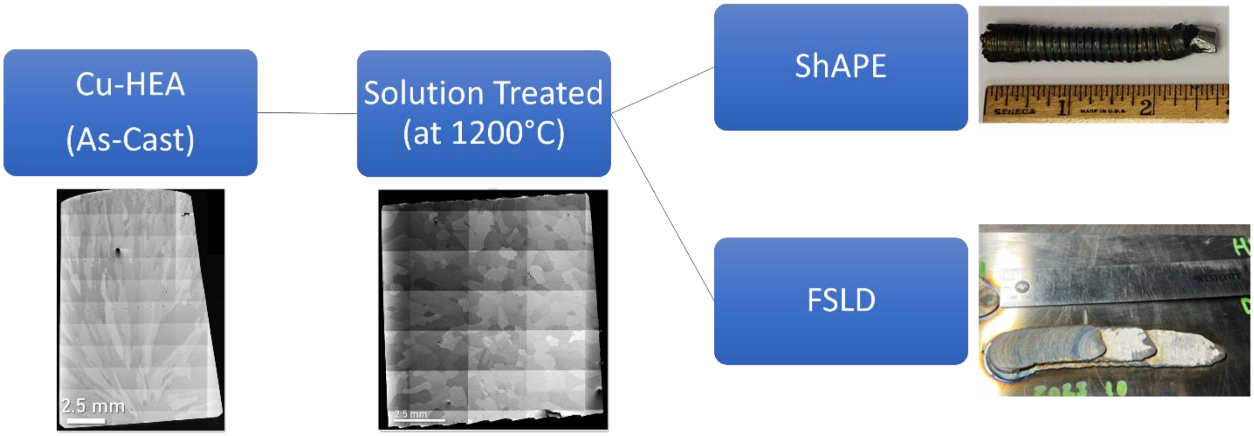

Figure 6. Flow-chart of heat treatment of Cu-HEA and solid-state processing routes.

1.3.3 Physical Properties of Cu-HEA

Figure 7 shows the physical properties that were measured for the Cu-HEA from room temperature to 1,000°C. Laser flash analysis (LFA) measurements were conducted on Cu-HEA to determine the thermal diffusivity of the Cu-HEA. The experiment was carried out using Netzsch LFA 457 at Idaho National Laboratory (see Appendix A for the detail). The sample had a diameter of 12.7 mm and thickness of 1.95 mm. The samples were heated from room temperature to 1,000°C at a heating rate of 3 K/min, and three individual samples were taken at each temperature. Figure 7(a) shows the change of thermal diffusivity with temperature for the Cu-HEA. It seems the slope changed around 700°C, which may correspond to the phase change in the alloy. Figure 7(b) shows the evolution of heat capacity with increase in temperature in the alloy. The sample was evaluated in a differential scanning calorimeter DSC at a heating rate of 10 K/min. DSC parameters held constants for all samples. Figure 7(c) shows the thermal conductivity values at different temperatures for this alloy. The following equation was used to calculate the thermal diffusivity from the experimentally measured thermal diffusivity and heat capacity:

$$K(T) = \alpha(T) \cdot C_P \cdot \rho$$

where K(T) is the thermal conductivity, α(T) is the thermal diffusivity, C_P is the specific heat and ρ is the bulk density of the HEA. The density of the HEA was considered as 8.8 gram/cm^3 from reported value [1].

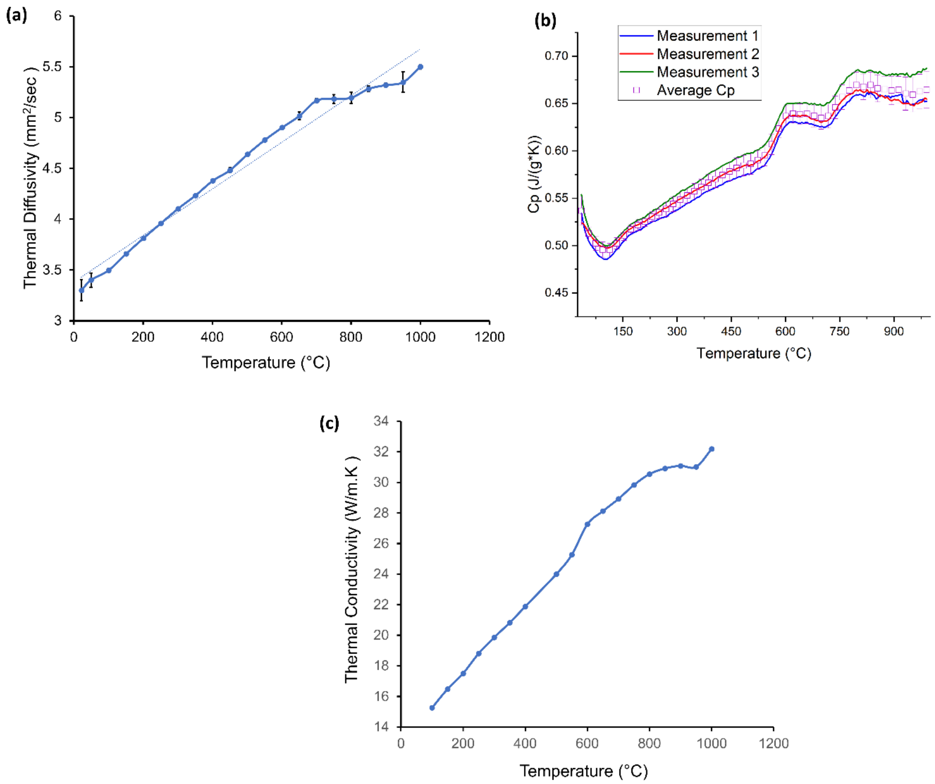

Figure 7. Graphs (a-c) are plots of the increase of thermal diffusivity, heat capacity, and thermal conductivity in the Cu-HEA with temperature, respectively.

Table 1. Average thermal diffusivity, heat capacity and thermal conductivity values for the Cu-HEA

Temperature (°C)	Thermal Diffusivity (mm^2/sec)	Standard Deviation	Heat Capacity (J/g*K)	Standard Deviation	Thermal Conductivity (W/m.K)
100	3.496	0.017	0.496	0.0066	15.26
150	3.659	0.019	0.512	0.0055	16.486
200	3.812	0.009	0.522	0.0055	17.51
250	3.958	0.007	0.540	0.0076	18.81
300	4.103	0.008	0.550	0.0086	19.86
350	4.233	0.012	0.559	0.0080	20.823
400	4.378	0.009	0.568	0.0092	21.883
500	4.638	0.005	0.588	0.0105	24
550	4.779	0.004	0.601	0.0105	25.275
600	4.901	0.013	0.632	0.0107	27.26
650	5.016	0.038	0.637	0.0111	28.12
700	5.167	0.018	0.636	0.0125	28.92
750	5.183	0.043	0.654	0.0129	29.83
800	5.195	0.057	0.668	0.0132	30.54
850	5.282	0.027	0.665	0.0136	30.91
900	5.319	0.021	0.664	0.0139	31.08
950	5.348	0.1	0.659	0.0182	31.014
1,000	5.5	0.024	0.665	0.0194	32.186

1.3.4 Baseline Corrosion Behavior

When developing new materials, it is important to be able to understand how the material will behave in corrosive environments. Due to the ubiquity of water across environments, it is important to understand how the material behaves in the presence of water. Testing in an autoclave allows acceleration of corrosion effects and reveals what surface chemistries develop as well as pathways for oxygen ingress into the bulk material. Performing electrochemical corrosion testing reveals corrosion mechanisms, limits, and provides a method of comparison for corrosion behavior across different alloys.

These two methods have been employed to provide a baseline understanding of the corrosion behavior of the HEA alloy used in this study. Testing was performed on as-cast samples and samples that have undergone homogenization. Homogenization was performed at 1200°C for 3 hours, followed by a cool-down period. This was then followed by another heating to 1,200°C for an additional 3 hours, followed by a quench in de-ionized water.

1.3.4.1 Aqueous Corrosion

Four samples were obtained for aqueous corrosion testing, two as-cast and two homogenized. One of each of the different samples was set aside for imaging while the other was placed into separate 300mL non-stirred, stainless steel pressure vessels. Samples were placed on an alumina spacer to insulate the sample from the stainless-steel vessel. The vessel was then filled with 200 mL of simulated the pressurized water reactor water (1,000 ppm B, 2 ppm Li, pH ~6.5). The vessels were sealed and placed into an oven which was heated to 275°C and held at temperature for 216 hours before being naturally cooled. After cooling all four samples were investigated using X-ray diffraction (XRD). After XRD analysis, the samples were mounted on edge into epoxy and polished to expose the cross-section for imaging on an SEM.

Optical images of samples were taken before and after exposure. After exposure, both samples went from a light silver to dark, almost black (Figure 8). Mass measurements were also taken of both samples before and after exposure. Neither sample showed any significant change in mass after exposure.

SEM images show that both the as-cast and homogenized samples (developed a surface layer that is approximately 0.5 µm on both samples. Both layers appear to be non-continuous, though the layer on the homogenized sample appears to be denser. Energy dispersive spectroscopy (EDS) analysis of the surface layer indicates that this surface layer contains aluminum. No Al-based polishes were used during polishing, and since the apparent Al shows up on both surface it is unlikely that it is contamination from the alumina spacer. The presence of Al in defects and inclusions that appear in the sample (see Figure 9, Figure 10 and Figure 11) further supports the idea that Al is present as an impurity in the raw material.

XRD results of all four samples from corrosion testing are shown in Table 2. The XRD analysis of the samples confirms the presence of Al on the surface of the corrosion samples in the form of $FeNiAlO_4$. All four samples showed the presence of Fe-Ni phases on the surface. The XRD results from as-cast sample also indicated the presence of iron-oxide while no oxide phase was indicated in the homogenized sample, instead a Fe-Co-Ni phase was present. Both corrosion samples showed the presence of phases containing Li and B from the pressurized water reactor simulated water. No Cr containing samples were found on the surface of any of the samples. Cu only appeared in the homogenized corrosion sample.

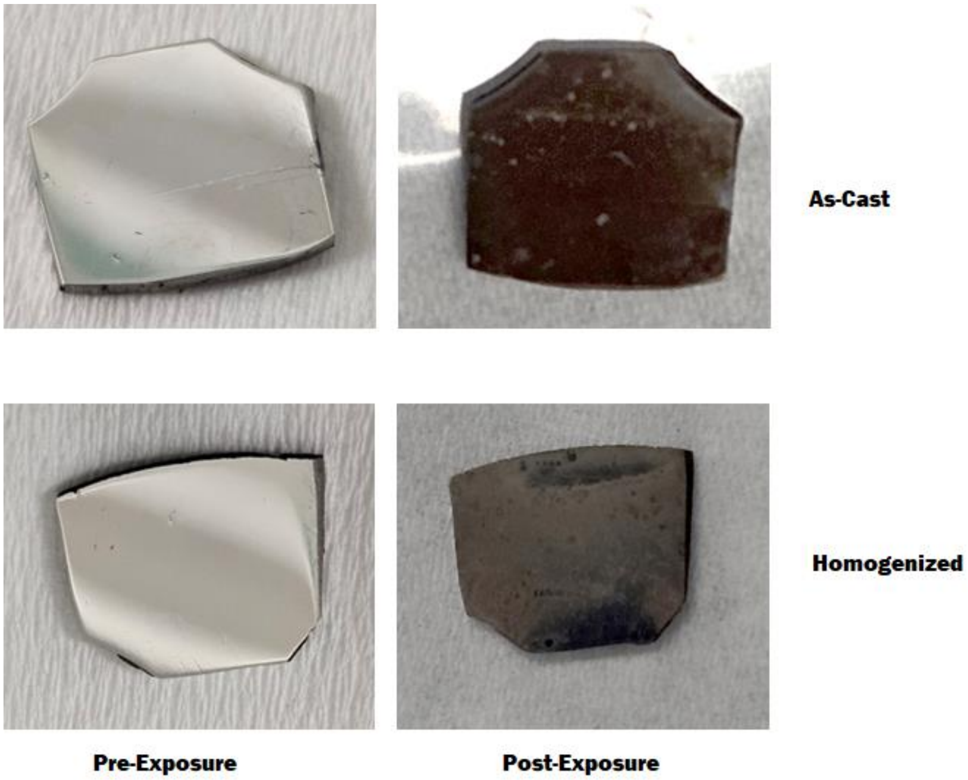

Figure 8. Optical images of samples before and after exposure in an autoclave

Table 2. XRD results of all four samples from corrosion testing

As-Cast	$Fe_{0.75}Ni_{0.25}$	As-Cast Corrosion	$Fe_{0.75}Ni_{0.25}$
			$Li_{6.52}B_{18}O_{0.26}$
	Fe_3O_4		$FeNiAlO_4$
			Co_3B
Homogenized	$Fe_{0.9}Ni_3$	Homogenized Corrosion	$Fe_{0.9}Ni_3$
			Fe_2O_3 (gamma)
			$FeBO_3$
	$Fe_{0.5}Co_{0.4}Ni_{0.1}$		$Co_4B_6O_{13}$
			$Li_8Cu_7B_{14}O_{32}$
			$FeNiAlO_4$

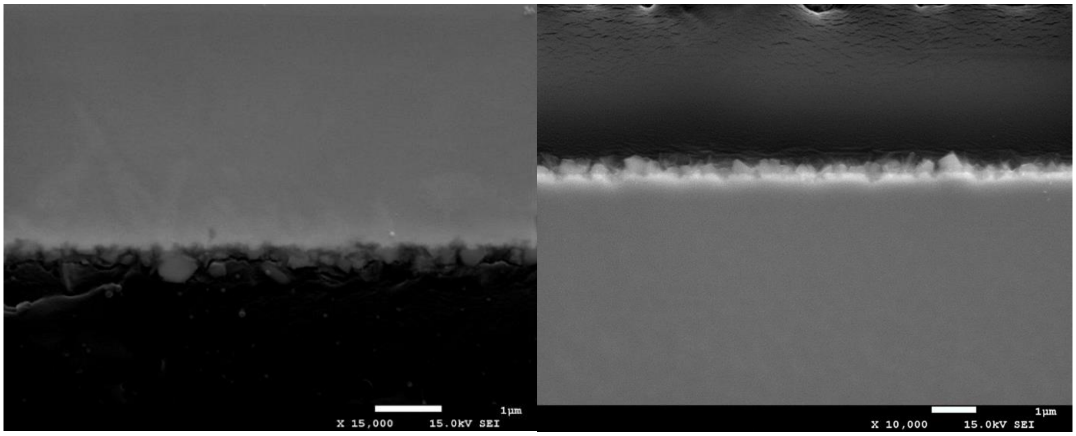

Figure 9. SEM image of surface of as-cast (left) and the homogenized (right) sample after exposure in an autoclave

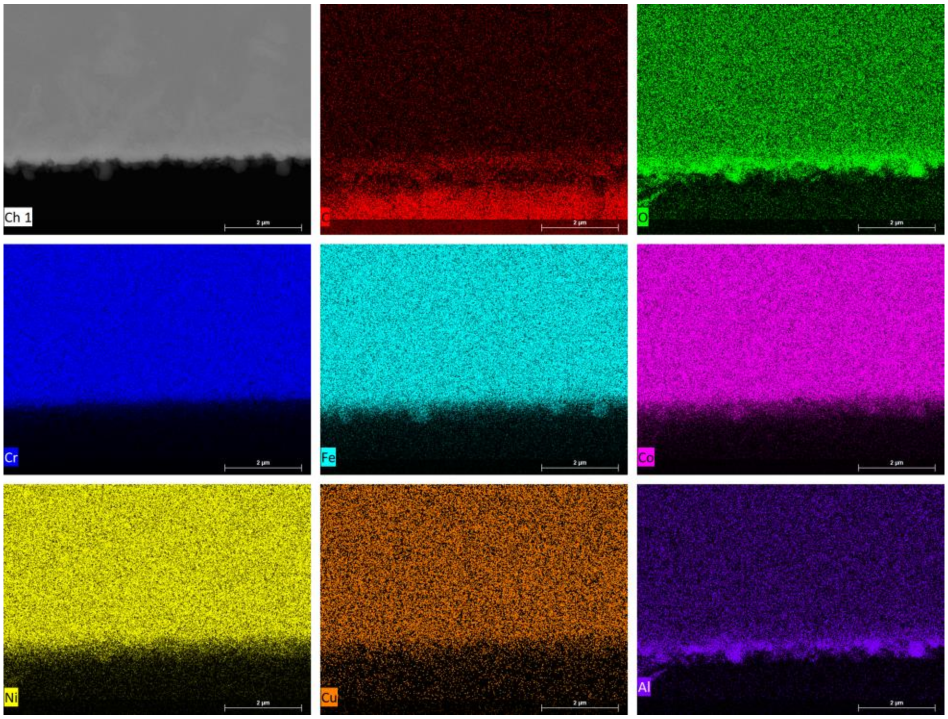

Figure 10. EDS maps of as-cast sample after exposure in autoclave

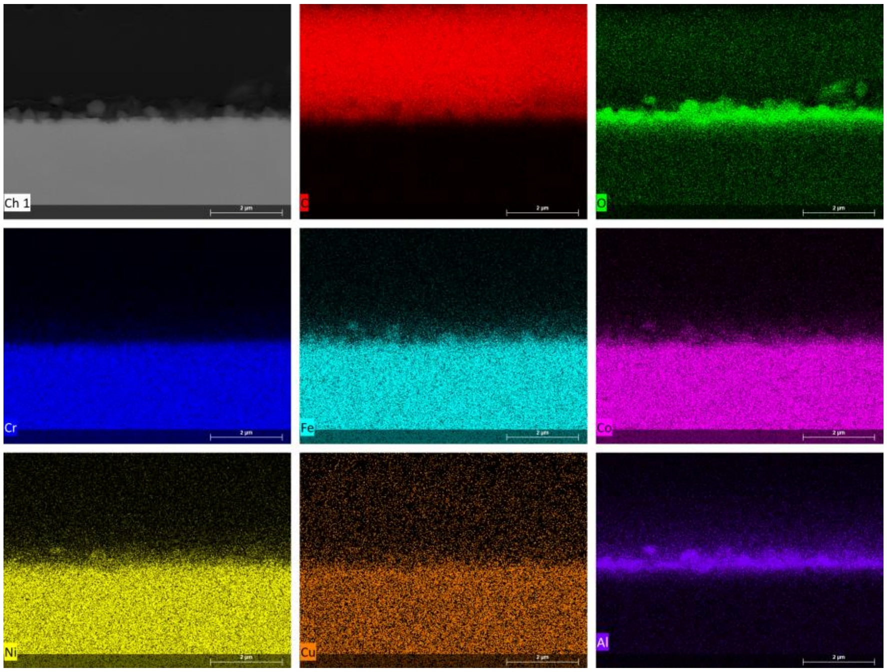

Figure 11. EDS results of homogenized sample after exposure in autoclave

SEM analysis of the as-cast samples revealed the presence of small defects in the material (Figure 12). These defects remained after heat treatment and corrosion. EDS analysis of the area (Figure 13) revealed that the edges were high in Cr and O, like what would be expected to be seen on an outer surface of the material. The homogenized corrosion sample had a significant defect that extended to the surface (Figure 12). EDS analysis (Figure 14) of the region did not seem to indicate any enhancement of corrosion effects, or penetration beyond the exposed channel. The analysis also showed Zr particles within the defect. It is possible that trace Zr was present in the fabrication of the material and was not fully homogenized during casting. While present in all samples, these defects are not prevalent throughout an individual sample and are not expected to impact the performance of the material. The homogenized samples also developed inclusions within the bulk. The inclusions seem to primarily be composed of Cr and O (Figure 15). The presence of Si could be from the polishing compound used. These inclusions developed in the bulk material and were not exposed to air during homogenization. That these inclusions are oxides seems to indicate that oxygen is present in the bulk matrix at the time of fabrication

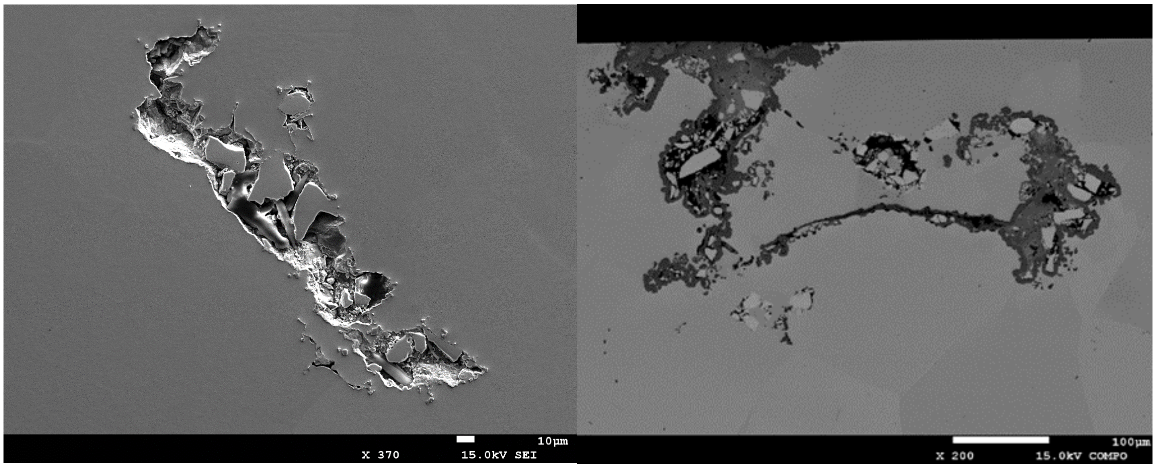

Figure 12. SEM image of defect in as-cast (left) and homogenized (right) corrosion samples

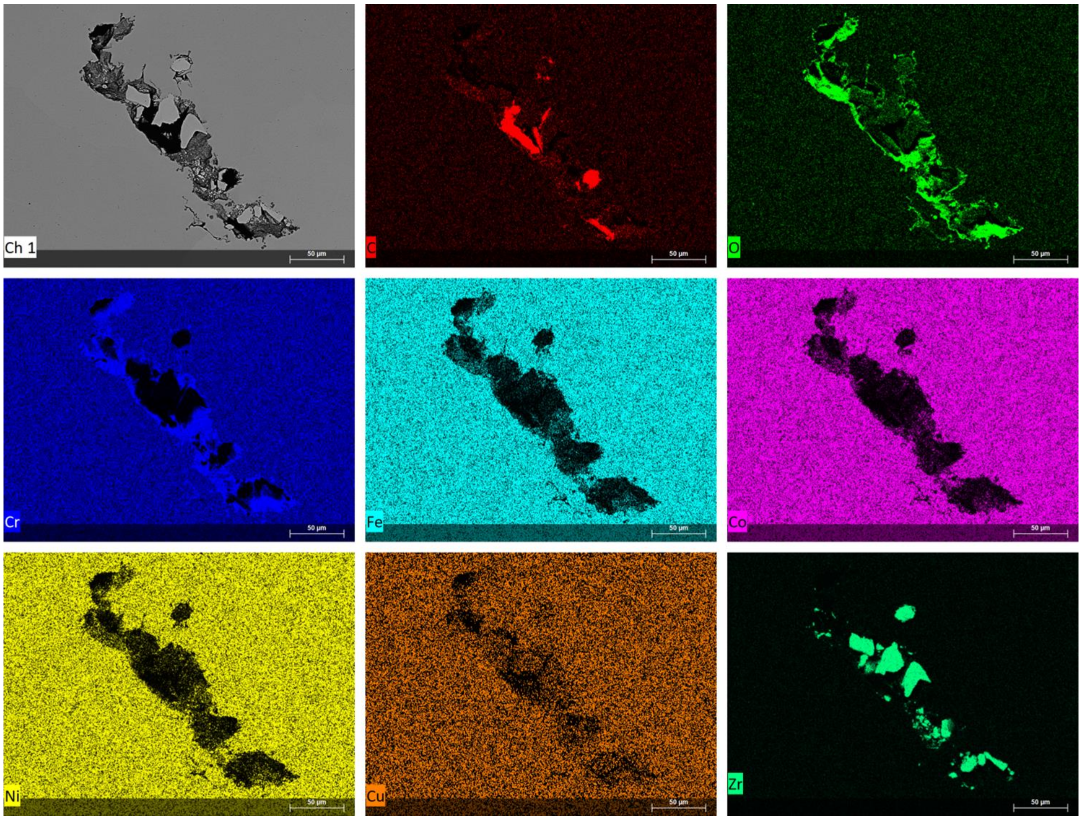

Figure 13. EDS map of defect in as-cast sample

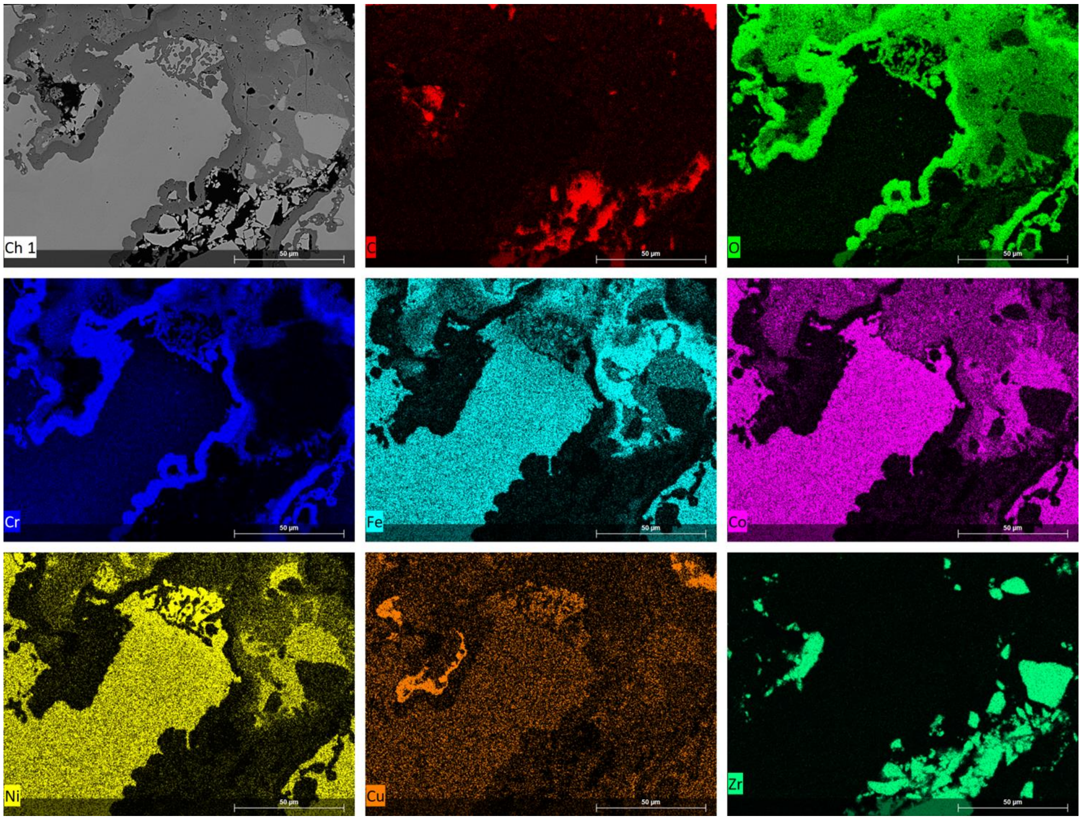

Figure 14. EDS map of defect in homogenized corrosion sample

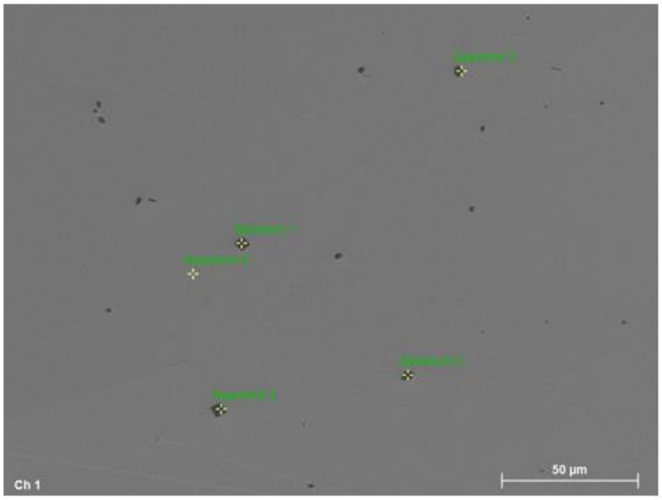

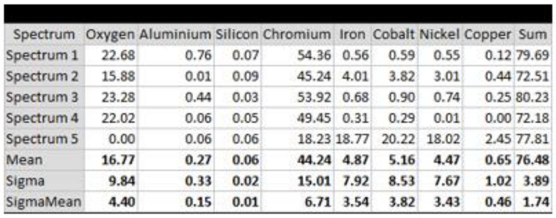

Spectrum	Oxygen	Aluminium	Silicon	Chromium	Iron	Cobalt	Nickel	Copper	Sum
Spectrum 1	22.68	0.76	0.07	54.36	0.56	0.59	0.55	0.12	79.69
Spectrum 2	15.88	0.01	0.09	45.24	4.01	3.82	3.01	0.44	72.51
Spectrum 3	23.28	0.44	0.03	53.92	0.68	0.90	0.74	0.25	80.23
Spectrum 4	22.02	0.06	0.05	49.45	0.31	0.29	0.01	0.00	72.18
Spectrum 5	0.00	0.06	0.06	18.23	18.77	20.22	18.02	2.45	77.81
Mean	**16.77**	**0.27**	**0.06**	**44.24**	**4.87**	**5.16**	**4.47**	**0.65**	**76.48**
Sigma	**9.84**	**0.33**	**0.02**	**15.01**	**7.92**	**8.53**	**7.67**	**1.02**	**3.89**
SigmaMean	**4.40**	**0.15**	**0.01**	**6.71**	**3.54**	**3.82**	**3.43**	**0.46**	**1.74**

Figure 15. EDS analysis of inclusions in homogenized sample

1.3.4.2 Electrochemical Corrosion

Electrochemical corrosion testing was performed on 16mm disks in a 0.5M H_2SO_4 solution at ambient temperature using an Ag/AgCl reference electrode. Samples were polished to at least a 1 µm surface finish prior to testing. Six samples were provided for testing, three each of the as-cast and homogenized materials.

Testing of the open current potential of both materials showed that the as-cast material was slightly more noble than that of the homogenized sample, or that the homogenized sample was more susceptible to corrosion than the as-cast material (Figure 16).

Anodic potentiodynamic polarization testing was performed in accordance with ASTM G5 standards. The E_{corr} values of the as-cast and homogenized material were –3 mV (vs. Ag/AgCl) and -104 mV (vs. Ag/AgCl), respectively. The I_{corr} values of the as-cast and homogenized materials were 9.5E-8 A/cm^2 and 3.3E-7 A/cm^2, respectively. Potentiodynamic testing also showed that the corrosion potential of the homogenized material is slightly more negative (less noble) by about 100 mV (vs. Ag/AgCl) when compared to as-cast material. The corrosion current of the homogenized material is about an order of magnitude higher than the as-received material (Figure 17).

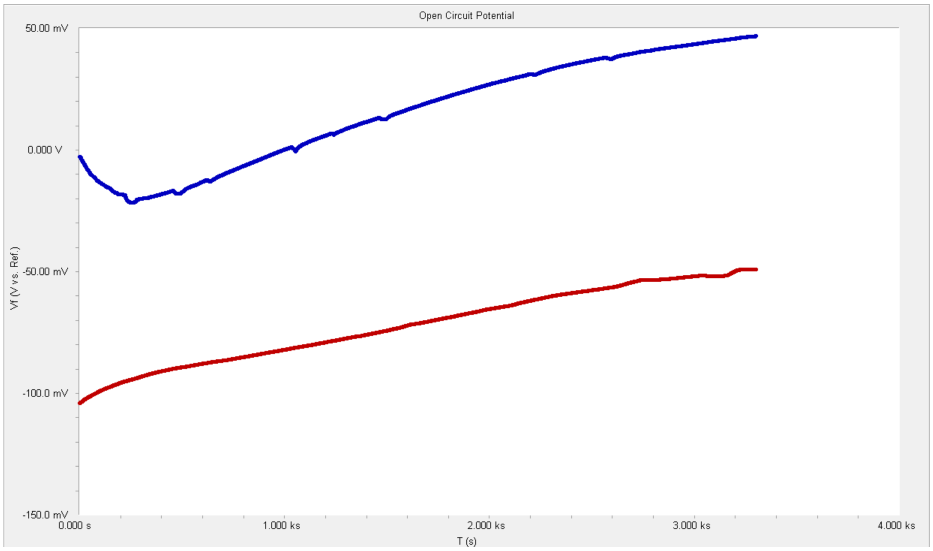

Figure 16. Open current potential for as-cast sample (blue) and homogenized sample (red)

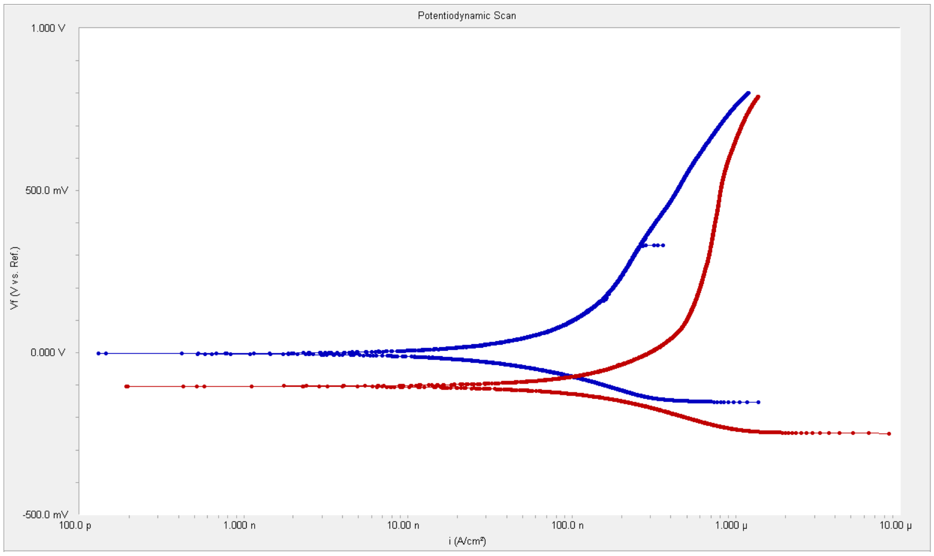

Figure 17. Potentiodynamic polarization curves for the as-cast (blue) and homogenized (red) samples.

2.0 Phase 1: Direct Tube Manufacturing of the Irradiation-resistant HEA Composite with Increased Strength

2.1 Initial SPH Modeling to Identify ShAPE Process Parameter Window

Predictions from the SPH modeling were used to inform the processing parameters for the initial experiments to keep the extrusion force and torque within machine limits. Multiple ShAPE cases were modeled with different die advance per revolution (APR) (e.g., die advancing speed/rotational speed). First, the model-predicted material morphologies of a small, extruded tube section in the extrusion direction for cases 1, 2, 3, and 5 are compared with measured material helical angles, as shown in Figure 18. When the APR is low, say 0.5 for case 1, a clear helical material pattern can be seen with 74.1° angle to the extrusion direction. With a lower ARP, say 0.25 for cases 2 and 4, the helical angles increased to 82.1° and 79.6°, respectively. This is as expected because a lower die APR indicates more die revolutions per unit extrusion length. As a result, the material helical pattern is prone to being more vertical. If the APR was further reduced to 0.167 in cases 3 and 5, billet material is well mixed by the die rotation. In these cases, it is hard to distinguish the helical angles which are obviously larger than 85°.

Figure 18 shows the model-predicted central cross-sectional temperature for cases 1, 3, and 5. When die plunging speed is fixed at 25 mm/min, increasing the die rotational speed from 50 revolutions per minute (RPM) (case 1) to 150 RPM (case 3) increases the overall heat generation and temperature in the billet. With the same APR of 0.167 and RPM of 50, reducing the die plunging speed from 25 mm/min (case 3) to 8.33 mm/min (case 5) significantly increases the temperature in the billet. These results show that even with the same APR, slower die plunging speed results in a higher temperature. This is because a lower plunging speed allows enough time for the generated heat to transfer and prorogate throughout the billet ring. Based on all simulation results, the process parameter window is 25 mm/min, 50–100 RPM to ensure a safe operation temperature ranging from 900 to 1,200°C.

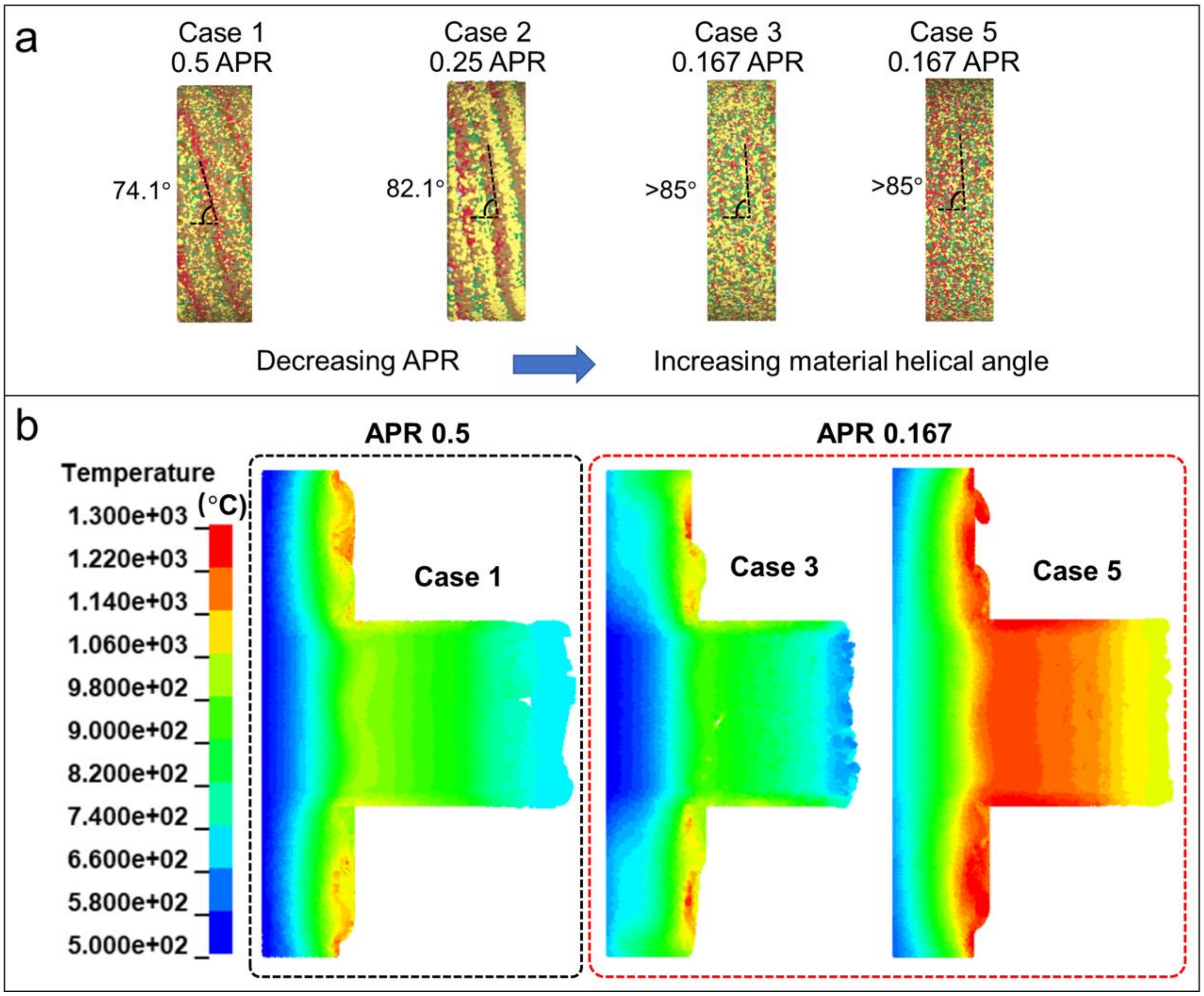

Figure 18. a) Model-predicted material morphologies of a small, extruded tube section in the extrusion direction for cases 1, 2, 3, and 5. b) Model-predicted central cross-sectional temperature for cases 1, 3, and 5

2.2 Die Design for NiCoFeCrCu$_{0.12}$ ShAPE Tube Fabrication

For the initial experiment, the die design was chosen as the standard geometry that is commonly used for ShAPE tube extrusion. A photograph of the tooling is shown in Figure 19. To withstand the high temperatures and forces that would occur during extrusion, the die materials were carefully chosen and are also shown in Figure 19. For instance, extrusion die was fabricated from W-La22O3, and mandrel, liner, backing block, and backer were made from Inconel 718.

Figure 19. Photograph of extrusion tooling and materials. IN refers to Inconel.

2.3 ShAPE Experimental Process Parameter Window

Because this is the first ever extrusion of high-temperature HEA, even if the tooling is durable enough to withstand the high temperatures and forces during extrusion, there was some concern of the machine torque and force capacities to cause problems with the extrusion. Therefore, predictions from SPH modeling were used to inform the processing parameters for the initial experiments to keep the extrusion force and torque within machine limits. The range of parameters shown in Table 3 were selected from SPH modeling to provide the ideal processing conditions for the first ShAPE experiments.

Table 3. Parameter ranges selected using SPH for the first ShAPE experiments.

Feed Rate (mm/min)	Die Rotation Speed (RPM)	Advance Per Revolution (mm)	Steady-State Die Temperature (°C)	Steady-State Extrusion Force (kN)	Steady-State Torque (N-m)
25	50–100	0.25–0.5	900–1,200	167–272	309–391

The steady-state force and torque values predicted using SPH are well within the machine limits for this range of die rotation speeds and temperatures. Therefore, the goal feed rate and rotation speed were chosen to be 75 RPM and 25mm/min.

2.4 ShAPE Experimental Execution

However, for the first set of experiments, a slower feed rate was chosen at 4 mm/min out of caution. Based on previous experience of extruding ODS2000 steel (performed for the DOE Office of Nuclear Energy's Advanced Materials and Manufacturing Technology program) where the steady state die rotational speed was maintained at 400 RPM, the rotational speed was selected as 200 RPM. The process response from this experiment is shown in Figure 20(a,b). During this experiment, the temperature increased much faster than expected, so it was aborted quickly.

The tooling was undamaged and only 0.5 mm was plunged into the billet, so the experiment was restarted with a lower initial rotation speed of 75 RPM and would be varied manually if necessary to control temperature and keep the torque within machine limits. This second trial was much more successful. The process response is shown in Figure 20(c,d), and a picture of the extrudate leaving the die is shown in Figure 20(e).

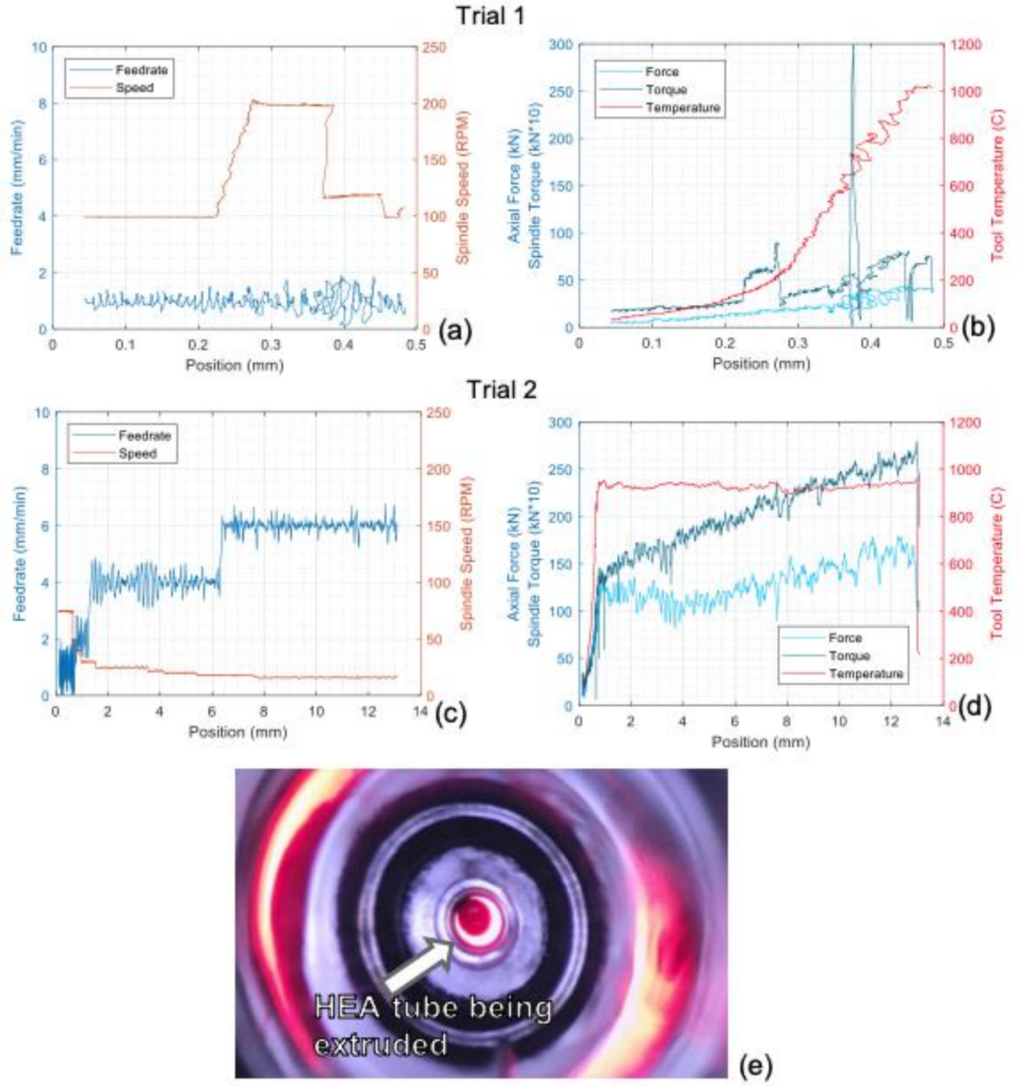

Figure 20. Process response of the initial ShAPE experiment, and a photograph of the HEA tube being extruded

As can be seen in Figure 20, the extrusion ramped slowly to the steady-state feed rate of 4 mm/min and the initial rotation speed was set to 75 RPM. However, the die temperature still increased at a high rate, so the rotation speed was manually reduced to 15-25 RPM for the remainder of the extrusion. The feed rate was also manually increased to 6mm/min because the extrusion force was well within machine limits. After some extrusion time, it was noticed that the torque was slowly approaching the machine limit of 3000 N-m and the tool appeared to be severely damaged, and the extrusion experiment was aborted.

A photograph of the damaged tooling is shown in Figure 21(a,b). This damage unfortunately prevented additional experiments for instance at the higher feed rates. Note that while the machine response was extremely different from the SPH predictions, the high torque and temperature response even with low rotation speed was likely caused by friction between the damaged tool and the liner, something that ordinarily would be avoided. However, the shortened extrusion did produce a small length of HEA tube, which is shown in Figure 21(c).

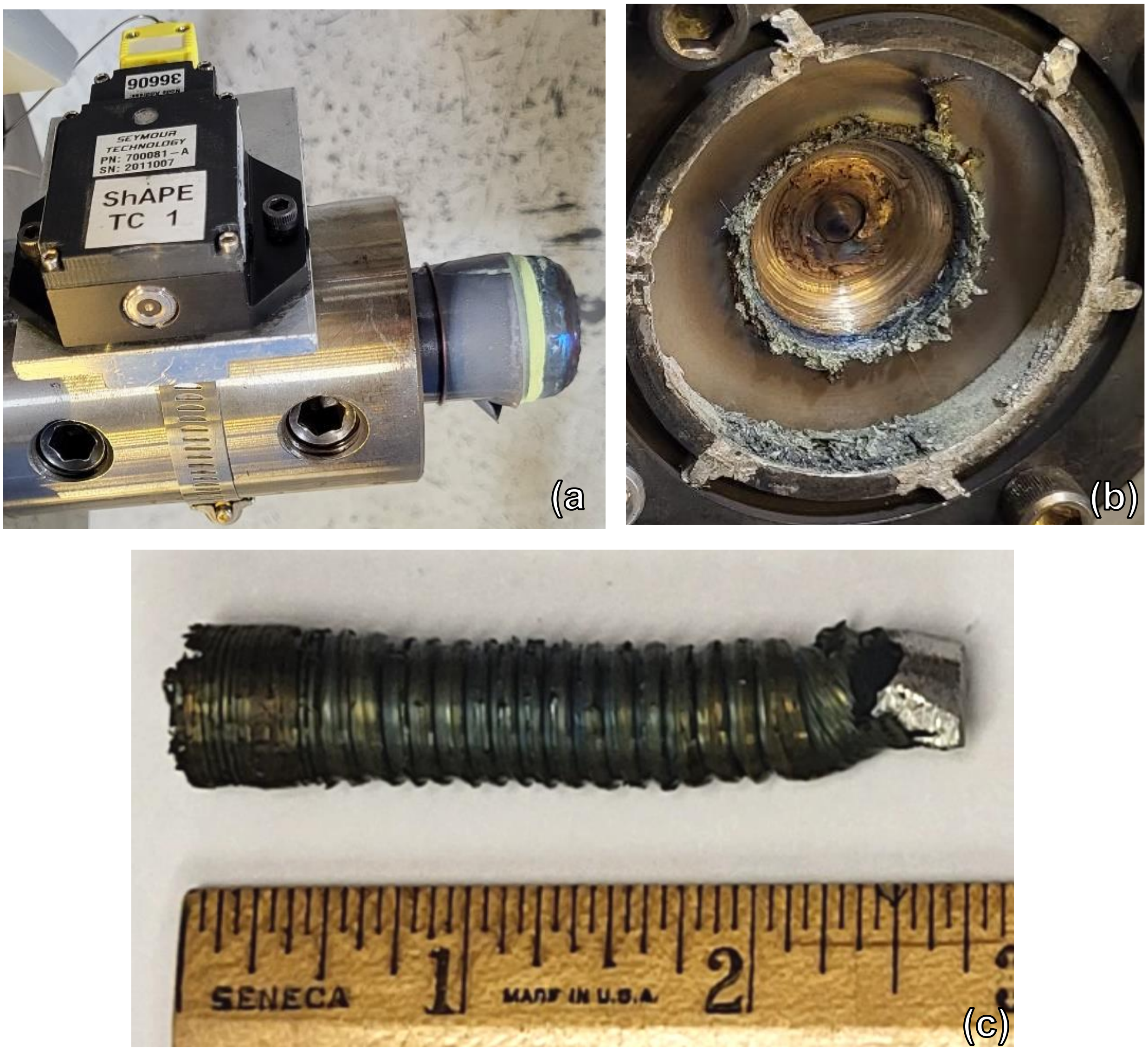

Figure 21. Photograph of the damaged tooling and the HEA ShAPE extruded tube segment

2.5 Comparing ShAPE Experimental Outcome with SPH Modeling Design

Even though the first-ever ShAPE extruded HEA tube was produced with 25 RPM and 6 mm/min, which is outside the model-suggested process parameter window of 25 mm/min, 50–100 RPM, a preliminary comparison was carried out between simulation and experiment in terms of material morphology. To this end, an SPH result was selected with 100 RPM and 25 mm/min, whose APR is 0.25 and is close to the 0.24 APR of the experiment. The image in Figure 22c shows that the SPH result reveals a helical material flow pattern that is very similar to the undulation on the HEA tube, thus validating the model capability in predicting accurate material flow. This gives confidence to further improve the SPH model and fill the prediction gap between simulation and experiment in the future.

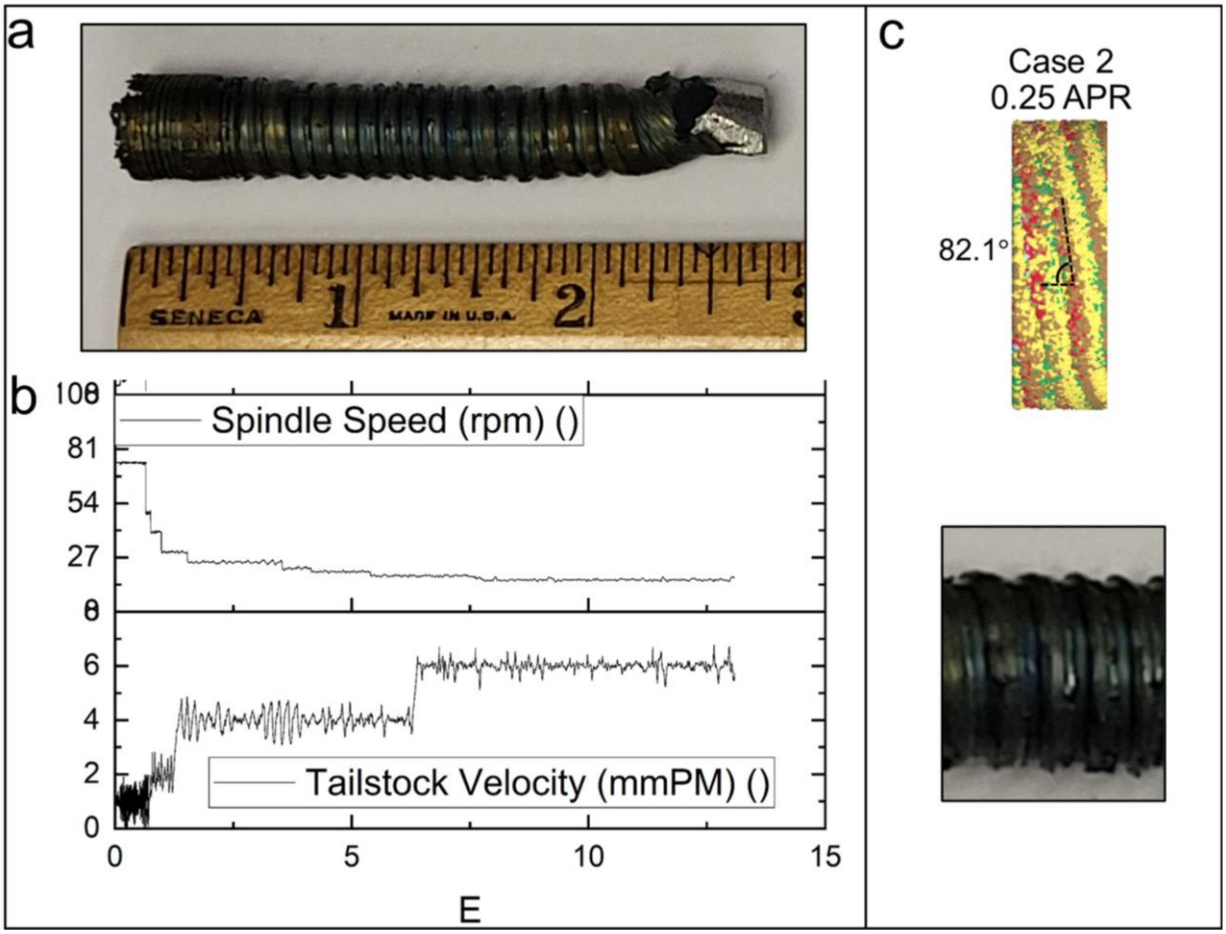

Figure 22. a) Fabricated ShAPE tube, b) fabrication parameters, and c) SPH result reveals a helical material flow pattern that is very similar to the undulation on the HEA tube, thus validating our model capability in predicting accurate material flow

Figure 23 compares the model-predicted process conditions vs. experimental data. The simulated Case #2 with a similar APR as the one used in experiment was used for comparison. The three images on the bottom show the comparison between simulation and experiment in terms of die temperature, extrusion force, and torque. The model-predicted temperature and force are slightly higher than the experimental data. This may be caused by the inaccurate temperature-dependent material property and thermal conditions used in the current SPH model, which can be better calibrated using the experimental data in the next step.

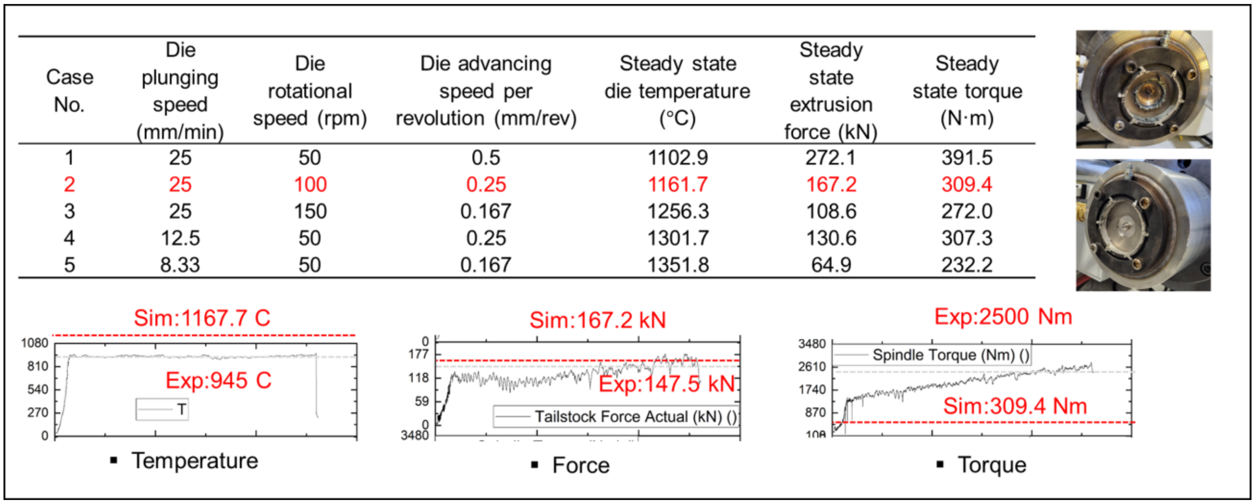

Case No.	Die plunging speed (mm/min)	Die rotational speed (rpm)	Die advancing speed per revolution (mm/rev)	Steady state die temperature (°C)	Steady state extrusion force (kN)	Steady state torque (N·m)
1	25	50	0.5	1102.9	272.1	391.5
2	25	100	0.25	1161.7	167.2	309.4
3	25	150	0.167	1256.3	108.6	272.0
4	12.5	50	0.25	1301.7	130.6	307.3
5	8.33	50	0.167	1351.8	64.9	232.2

Figure 23. Comparison of the model-predicted process conditions vs. experimental data. The simulated Case #2 with a similar APR as the one used in experiment was used for comparison

Moreover, we see a continuously increasing spindle torque from the experimental log, which is caused by the excessive flash generated during the ShAPE, as shown in Figure 22 and Figure 23. This is the main reason why torque is so underpredicted by the SPH model. By improving the SPH model and the application of better process parameters in the experiment, we believe the discrepancies between simulation and experiment can be significantly reduced.

2.6 Microstructural Characterization

A JEOL 7600 SEM was used to produce images and orientation mappings of the polished samples. Both backscatter electron and secondary electron imaging were used for microstructural characterization. Electron backscatter diffraction (EBSD) analysis was performed using AZtecCrystal software from Oxford Instruments.

Figure 24 shows the image of the ShAPE processed Cu-HEA that is nearly 2.5 inches in length. The sample was cut into three sections named ‘Start,’ ‘Middle,’ and ‘End’ to understand the role of various process parameters on microstructural evolution. Both transverse and longitudinal samples were prepared from each section for characterization. These samples had unique six-digit IDs as shown in the Figure 24. In this section, the microstructural information including SEM images and EBSD maps on all six samples have been presented.

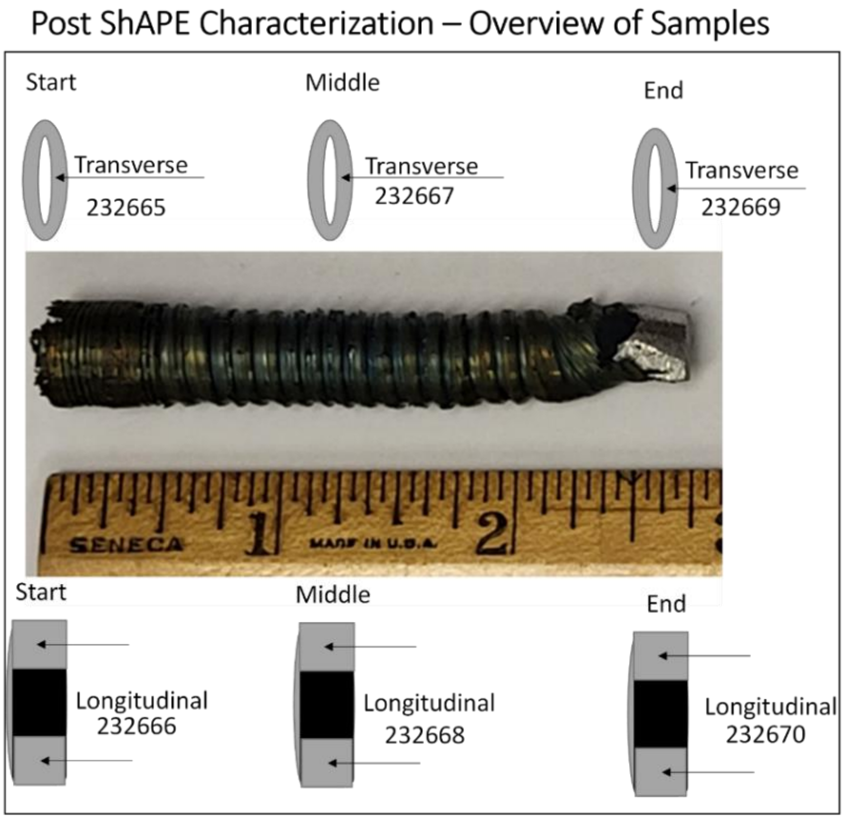

Figure 24. Schematic of sample cut plan for characterization on ShAPE processed Cu-HEA

2.6.1 Microstructural Characterization of “Start Section” Sample

Figure 25(a) shows the mount of the Start section and the spot for microstructural analysis of the transverse section has been highlighted in the red box. Figure 25(b-c) show SEM images with different magnifications that clearly show the grain structures. The presence of large number of twin boundaries in the grains can be attributed to high number of mechanical stresses and elevated temperatures of ShAPE processing. Figure 25(d) shows the inverse pole figure (IPF) map generated by orientation mapping in this sample considering the matrix to be of FCC in crystal structure. The IPF clearly shows the presence of significantly finer grains as that compared to that in pre-ShAPE sample (Figure 6). Figure 25(e) shows the plot of distribution of grain sizes (extracted from EBSD maps) in this sample that shows the mean grain size of 7.82 with a standard deviation of 2.61. The grain sizes of all six samples are provided in Table 4.

Table 4. Change in grain sizes across the length of the Cu-HEA sample after ShAPE processing

Sample	Grain Size (µm)	
	Longitudinal	Transverse
Solution-treated	660 ±21.8	
Start section- ShAPE	5.09 ±1.75	7.82 ±2.61
Middle Section	3.25 ±.92	3.37 ±1.21
End Section	4.04 ±1.4	4.56 ±1.58

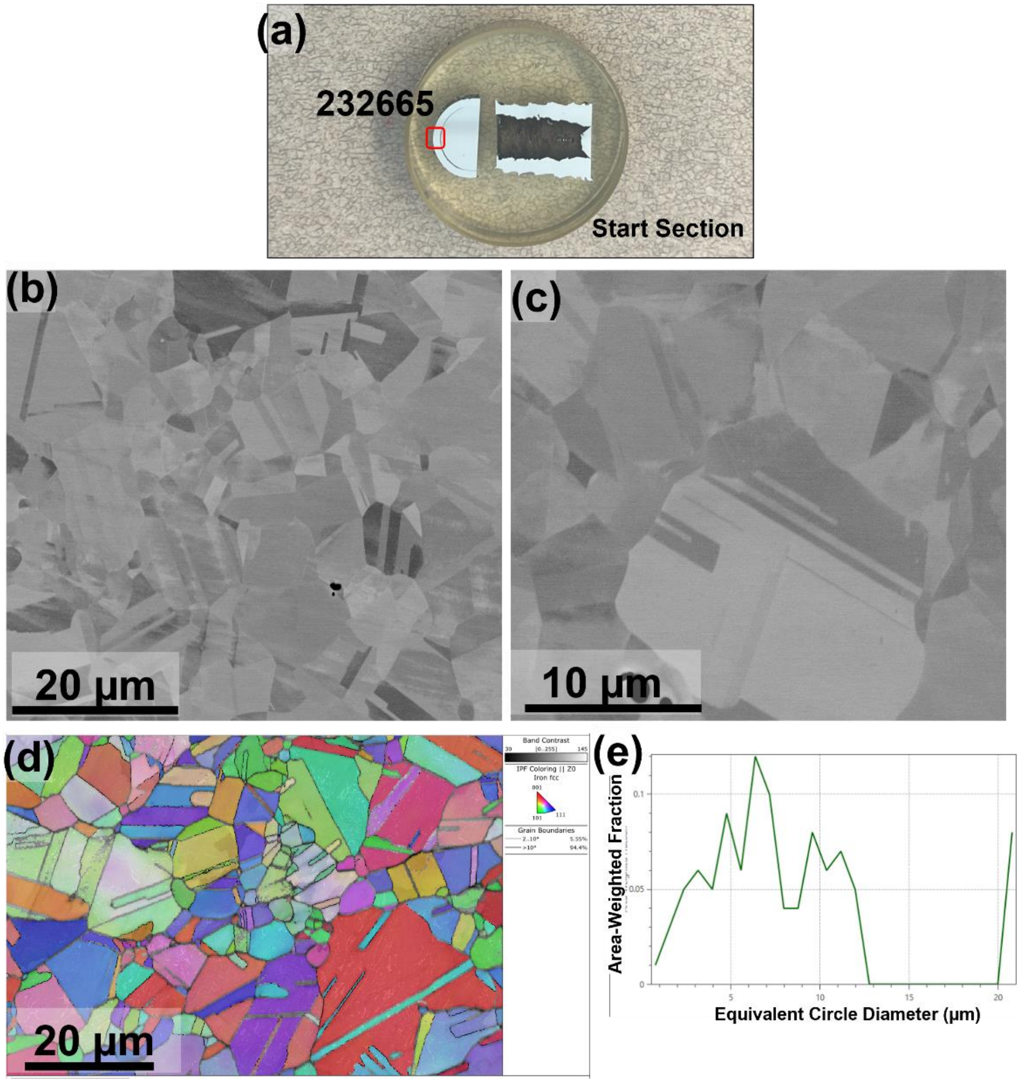

Figure 25. (a) Photograph of the mount indicating the transverse section of the ‘Start section’ by a red box. (b-c) SEM images from this transverse section with finer grain distribution. (d) IPF map of the FCC matrix that indicates the grain boundaries and twin boundaries distributions. (e) Plot of distribution of grain size obtained from orientation mapping.

While the ShAPE experiment ideally produces a hollow pipe structure, we found that the Start section of the extruded material has a central solid part. Figure 26(a) shows the mount of the Start section and the spot for microstructural analysis of such central region has been highlighted in the red box. Figure 26(b-c) show the SEM images with different magnifications that reveal the grain structures with grain boundaries precipitates. These precipitates were further investigated for their chemical compositions as shown in Figure 26(d), and we found that the precipitates are rich in elements such as Ni, Mo, Nb, and Ti. Although the Cu-HEA alloy does not contain Mo and Nb, the ShAPE experiments utilized IN718 (which contains Mo, Nb and Ti) as extrusion materials. Hence, it appears that the central part with the HEA extruded product is mostly the IN718 tooling material.

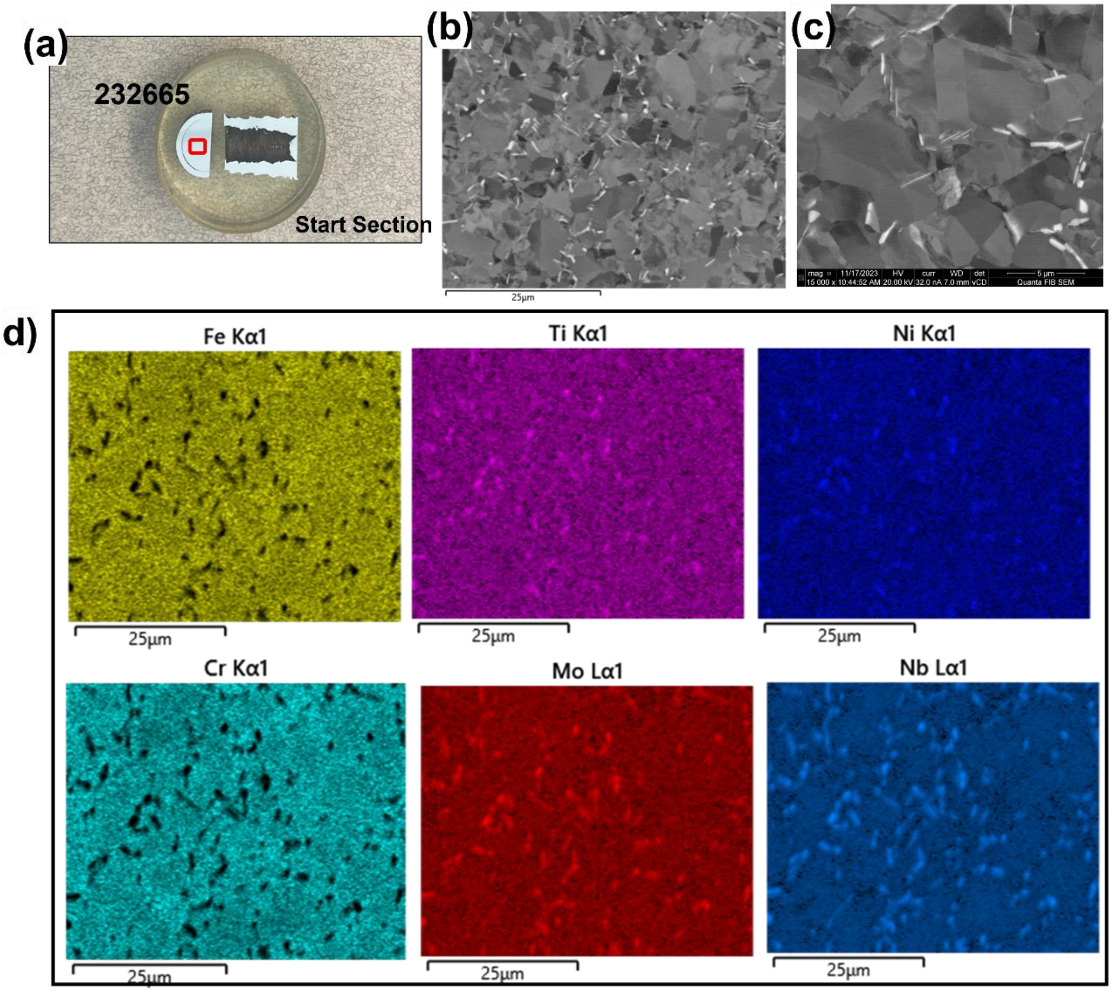

Figure 26. (a) Photograph of the mount indicating the ‘central region’ of the transverse section in the ‘Start section’ by a red box. (b-c) SEM images from this central region with finer grain distribution and grain boundary precipitates. d) Elemental chemical mapping from this region that shows the presence of Ti, Mo, and Nb in the grain boundary precipitates.

Figure 27(a) shows the mount of the Start section and the spot for microstructural analysis of the longitudinal section has been highlighted in the red box. The center of the longitudinal section is hollow and does not contain any tooling material. Figure 27(b-c) show SEM images with different magnifications that shows the grain structures. Figure 27(d) shows the IPF map generated by orientation mapping in this sample. Figure 27(e) shows the plot of distribution of grain sizes (extracted from EBSD maps) in this sample that shows the mean grain size of 5.09 µm. The longitudinal section seems to have lower grain size as compared to that in traverse section.

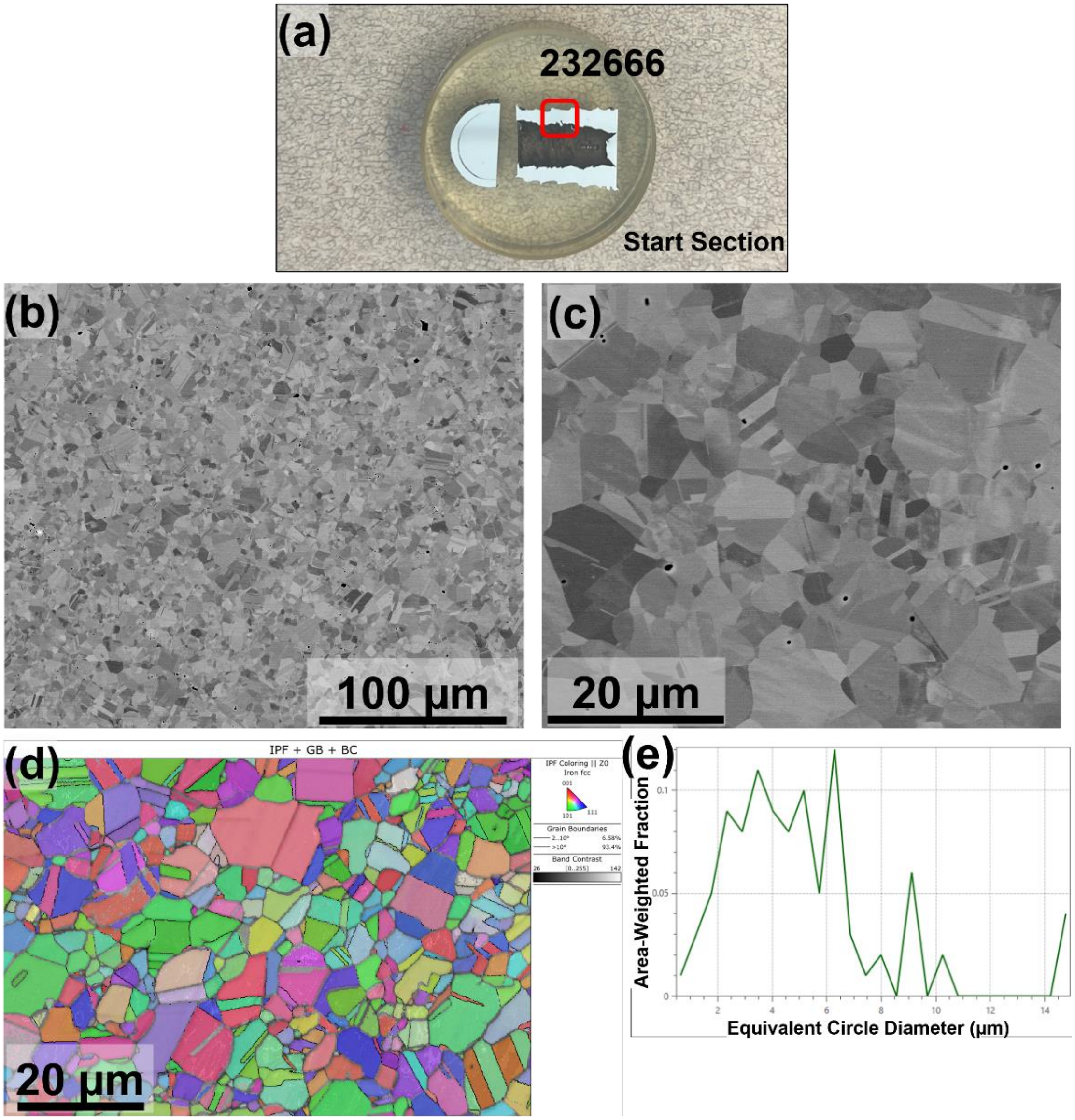

Figure 27. (a) Photograph of the mount indicating the longitudinal section of the ‘Start section’ by a red box. (b-c) SEM images from this longitudinal section with finer grain distribution. (d) IPF map of the FCC matrix that indicates the grain boundaries and twin boundaries distributions. (e) Plot of distribution of grain size obtained from orientation mapping.

2.6.2 Microstructural Characterization of “Middle Section” Sample

Similar to Start section of the ShAPE processed Cu-HEA, the Middle section was also characterized. Figure 28(a) shows the mount of the Middle section and the spot for microstructural analysis of the transverse section has been highlighted in the red box. The center of the transverse section is hollow and does not contain any tooling material. Figure 28(b-c) shows SEM images with different magnification that clearly shows the grain structures. The grain size information obtained from EBSD on Middle section has been provided in Table 4.

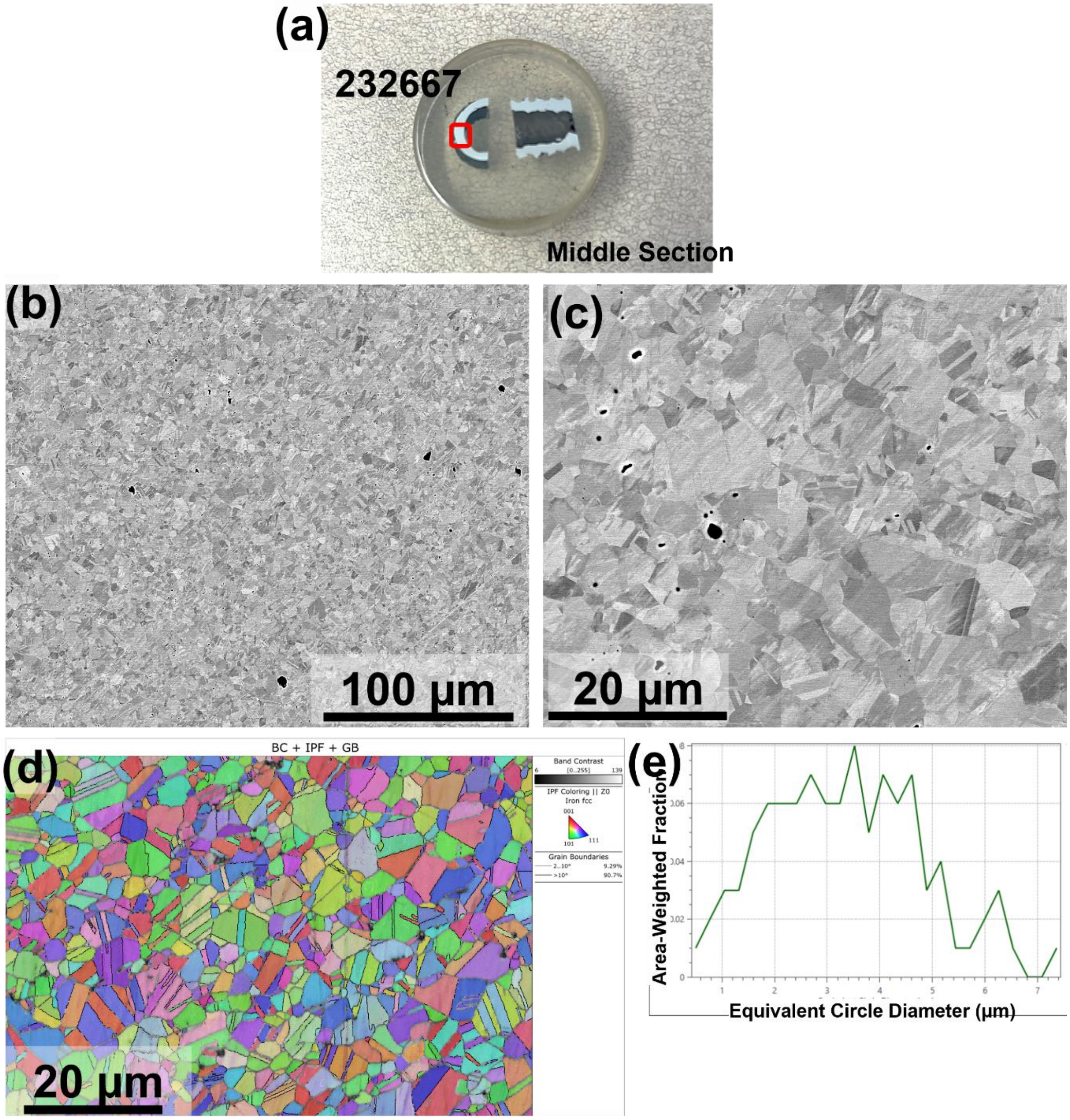

Figure 28. (a) Photograph of the mount indicating the transverse section of the ‘Middle section’ by a red box. (b-c) SEM images from this transverse section with finer grain distribution. (d) IPF map of the FCC matrix that indicates the grain boundaries and twin boundaries distributions. (e) Plot of distribution of grain size obtained from orientation mapping.

Figure 29(a) shows the mount of the Middle section and the spot for microstructural analysis of the longitudinal section has been highlighted in the red box. The center of the longitudinal section is hollow and does not contain any tooling material. The SEM images in Figure 29(b-c) and the IPF in Figure 29(d) show the finer grain structures.

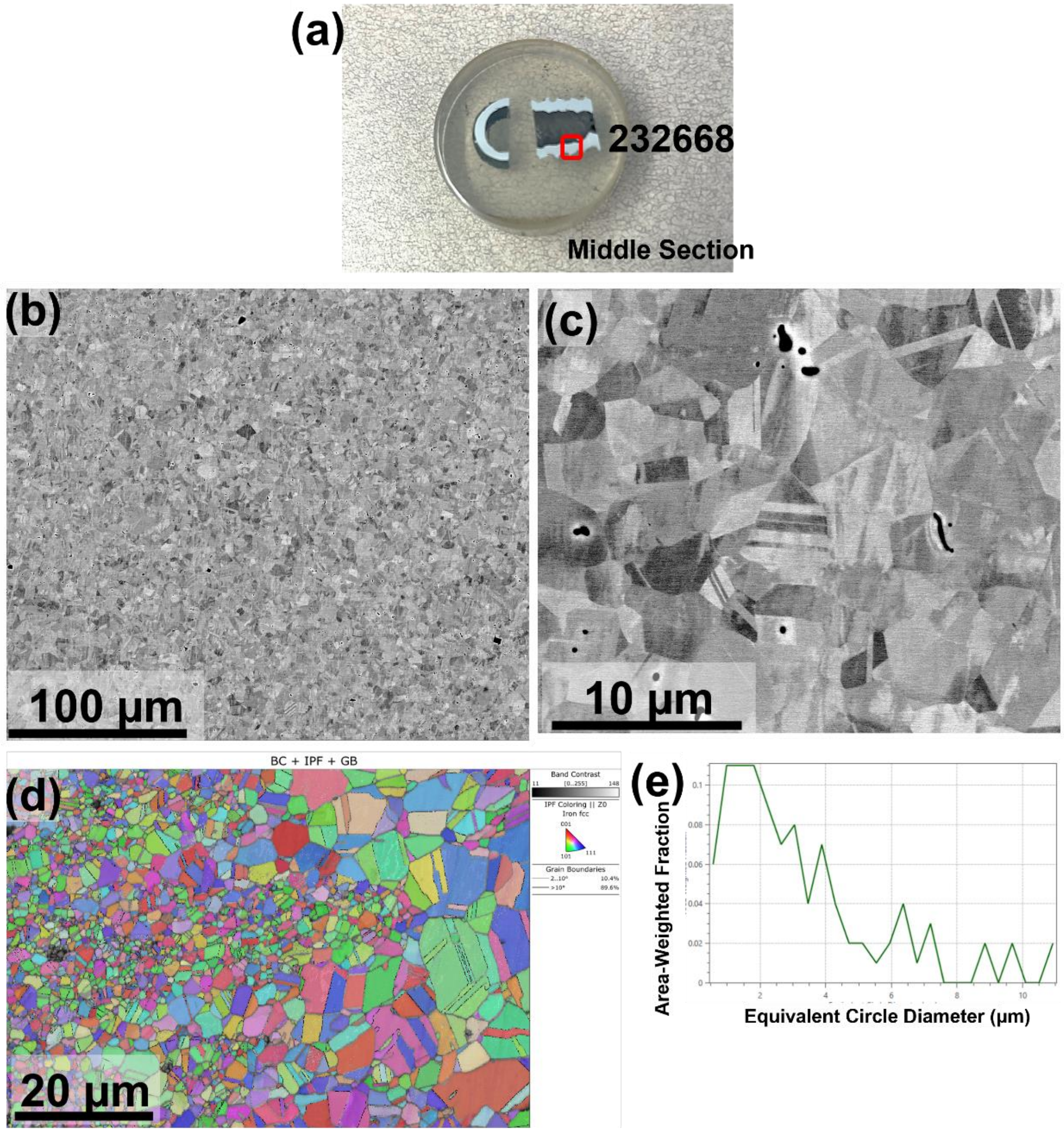

Figure 29. (a) Photograph of the mount indicating the longitudinal section of the 'Middle section' by a red box. (b-c) SEM images from this longitudinal section with finer grain distribution. (d) IPF map of the FCC matrix that indicates the grain boundaries and twin boundaries distributions. (e) Plot of distribution of grain size obtained from orientation mapping.

2.6.3 Microstructural Characterization of "End Section" Sample

Similar to Start section, the End section also contains the tooling material when the transverse section was analyzed, as shown in Figure 30(a). The grain size and distribution depicted by Figure 30 (b-e) are very similar to that in previous sections' traverse view.

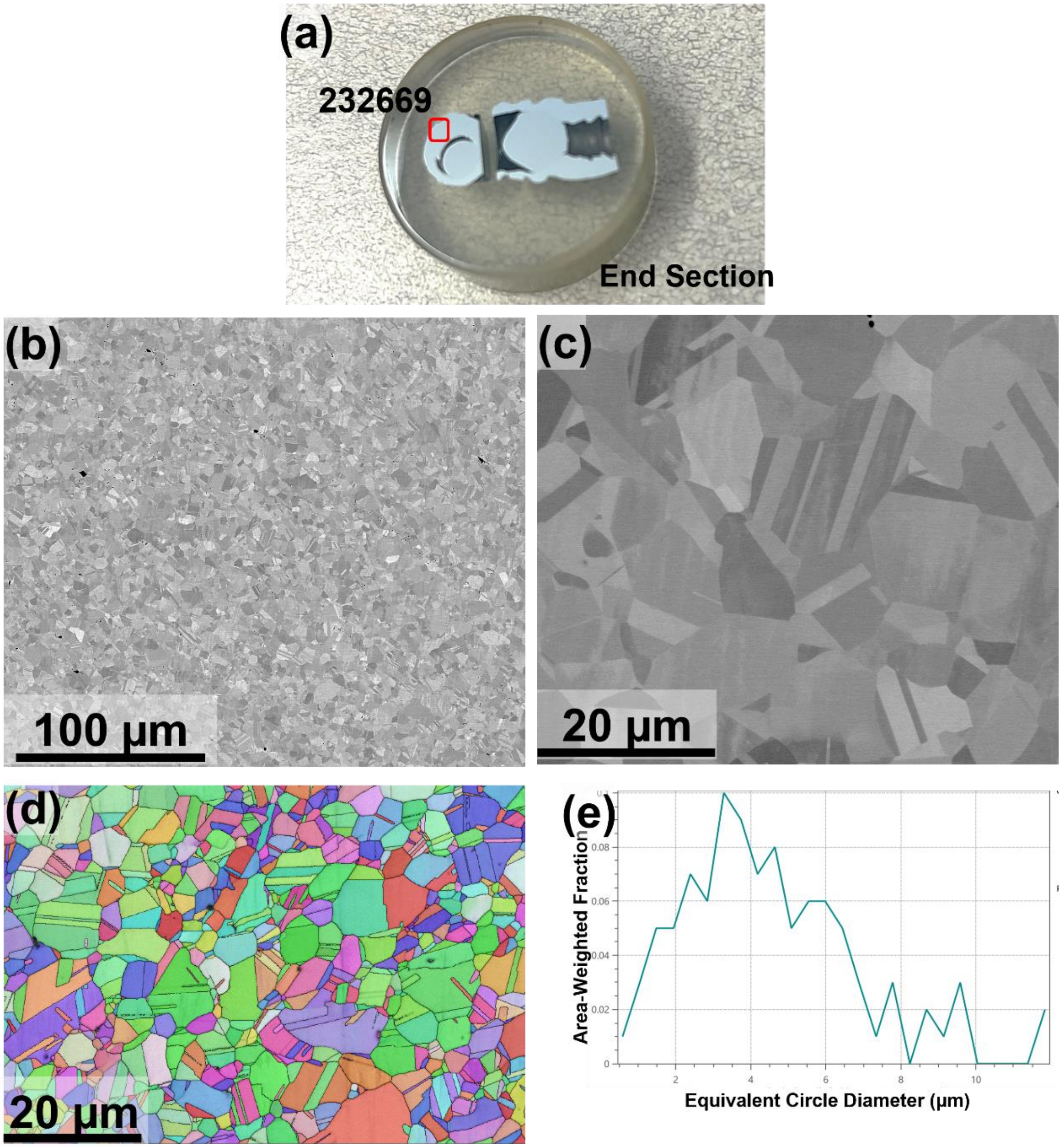

Figure 30. (a) Photograph of the mount indicating the transverse section of the ‘End section’ by a red box. (b-c) SEM images from this transverse section with finer grain distribution. (d) IPF map of the FCC matrix that indicates the grain boundaries and twin boundaries distributions. (e) Pot of distribution of grain size obtained from orientation mapping.

The longitudinal part of the End section seems to contain the tooling material within it, as shown in Figure 31(a). The grain size and distributions are presented in Figure 31(b-e) and Table 4. Table 4 shows the change in grain sizes across the length of the Cu-HEA sample after ShAPE processing.

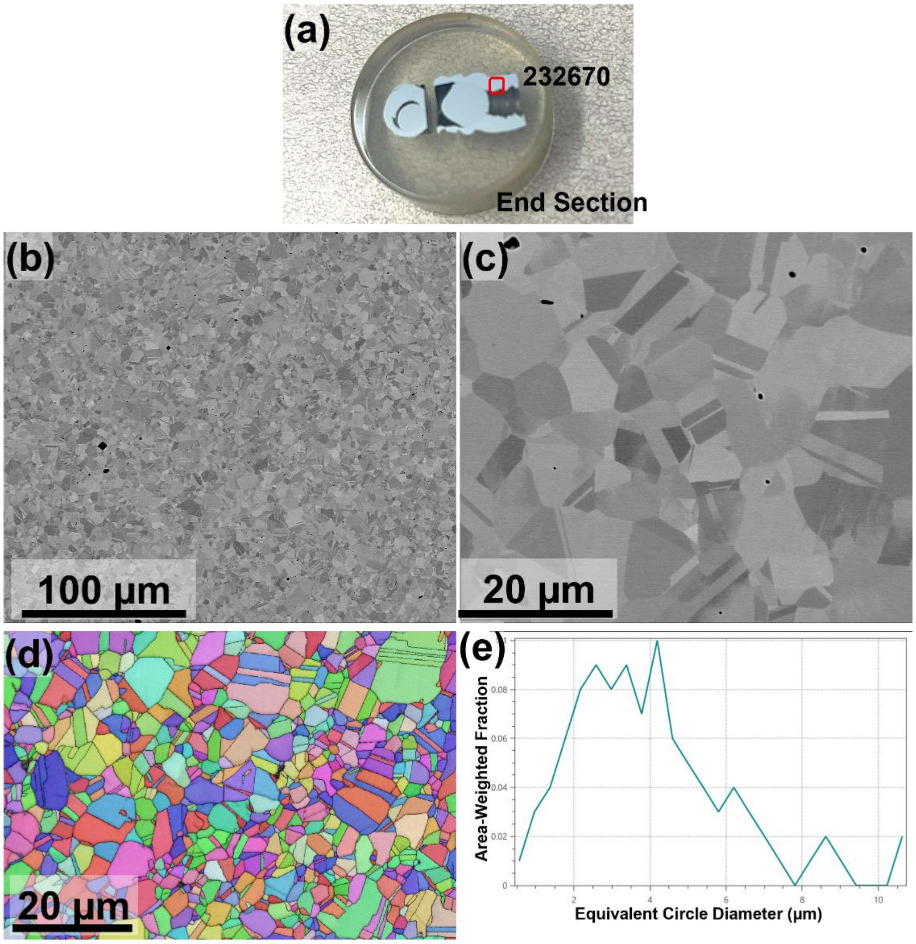

Figure 31. (a) Photograph of the mount indicating the longitudinal section of the 'End section' by a red box. (b-c) SEM images from this longitudinal section with finer grain distribution. (d) IPF map of the FCC matrix that indicates the grain boundaries and twin boundaries distributions. (e) Plot of distribution of grain size obtained from orientation mapping.

2.7 Hardness Measurements

The hardness testing was performed using a CLARK CM-802AT automatic hardness tester, and 300 gf of load was used. Figure 32(a-c) show the hardness values and the location of indents at various regions of Start, Middle and End sections respectively. The hardness values of the different parts of the extruded bar have been presented in Table 2. The hardness in ShAPE processed Cu-HEA is improved to an average HV value of 185 as compared to that of cast material (HV = 115). This enhancement of hardness is most probably due to grain boundary strengthening. It can be speculated from the moderate improvement of hardness value in ShAPE processed that the Cu-HEA in this process condition does not contain Cu-rich precipitates. Otherwise, there would have been a significant increase in hardness value in the extruded HEA tube.

The higher hardness of central part in the transverse sections of Start and End sections, as shown in Figure 32(a and c), are due to presence of the IN718.

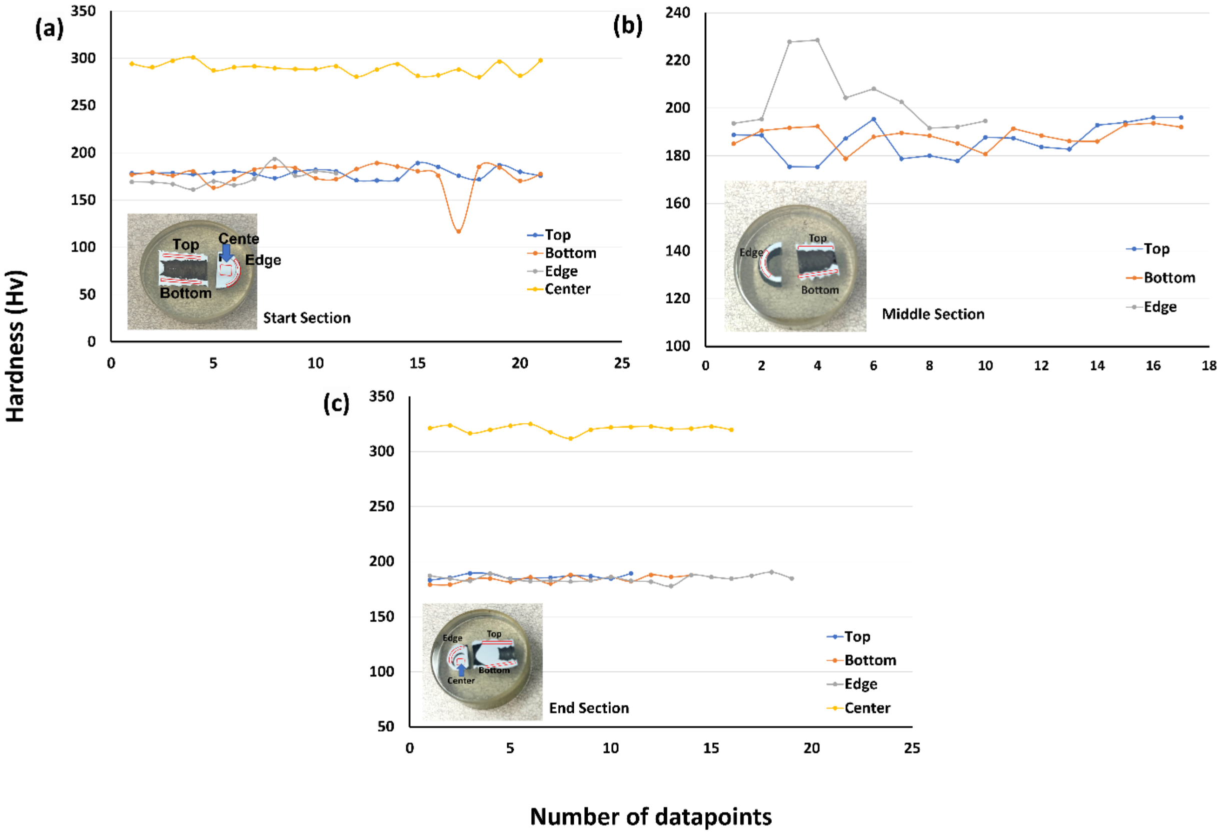

Figure 32. (a-c) Plots of hardness from various regions of Start, Middle and End sections respectively

Table 6 shows the changes in average hardness value across the length of the Cu-HEA sample after ShAPE processing.

Table 5. Changes in average hardness value across the length of the Cu-HEA sample after ShAPE processing

Sample	Average Hardness (HV)			
	Longitudinal		Transverse	
	Top	Bottom	Edge	Center*
Solution-treated	114.75			
Start section- ShAPE	178.24	177.05	172.92	289.72
Middle Section	186.32	188.27	203.84	Not present
End Section	186.41	183.98	184.54	320.54

*Contains tool material in the center as seen in Figure 26(a) and Figure 30(a)

2.8 Recommendation Based on First ShAPE Experiment and Characterization

Clearly, the tube produced in the initial experiment is not of production quality, but it does represent the first time a Cu-HEA was extruded using ShAPE or similar methods. The low quality extrudate and the torque issues were most likely caused by the mushrooming of the tool tip.

In future ShAPE experiments, the tool material will be changed to W-Re-HfC, which has a much higher strength at the temperatures at which the extrusion was done. The higher elevated temperature strength of this material should prevent mushrooming of the tool tip, which will keep the torque and temperature under much better control than experienced in the initial experiment. In addition to the tooling material change, the process parameters and tool design will be modified with input from the SPH model, which will be further refined using the results from the initial experiment.

The very first ShAPE experiment was completed using an indirect extrusion setup in which the extrusion die enters the liner, thereby leading to increased possibility of tooling failure. For instance, in the very first experiment, the die holder and chilled container were made from tool steel, and damage in the form of severe oxidation can be seen. Also, a new extrusion die made from W-La_2O_3 was compressed by almost 25 mm after the extrusion. Also, the mandrel made from IN718 was destroyed. Therefore, for the next set of experiments, a direct extrusion setup has been designed and is in the process of procurement. Furthermore, materials with increased temperature and force capability have been selected so that all the tooling sustains the extreme conditions experienced during extrusion of high temperature materials. The new set of tooling includes the following: 1) water-cooled die holder made from IN718, 2) extrusion dies made from W-Re-HfC since W-La_2O_3 extrusion die completely deformed during the first experiment, 3) a new larger chilled container assembly made from IN718, and 4) mandrels fabricated from W-La_2O_3 and W-Re-HfC. All these modifications were made so that the tooling survives the extrusion of the Cu-HEA.

Overall, the utilization of W-Re-HfC and W-La_2O_3 for dies and mandrels, and the completely new direct extrusion setup with increased temperature and force capabilities will lead to high-quality extrudates without destroying the costly tooling necessary to extrudate high performance materials via ShAPE.

3.0 Phase 3: ShAPE^{TM} of Radially Gradient Corrosion Resistance Alloy

Functionally graded materials also are considered as a potential solution for enhanced corrosion resistance should the current HEA alloy need additional corrosion protection in certain environments. In addition to the co-extrusion method explored in Phase 2, we evaluated a parallel effort using powder metallurgical routes to prepare the input billet for the ShAPE tube forming process. The hot isostatic press (HIP) technique was identified as one of the preferred options because of the high density billet it can provide, potentially leading to better quality tube with consistent properties as a final tube. Additionally, HIP is a solid-state manufacturing process; therefore, it provides additional advantages in maintaining the inner structure and preventing segregation. HIP [32] and spark plasma sintering [33,34] are the most advanced and popular powder metallurgy (PM) techniques currently available. Cold spray and associated friction stir layer deposition may be other solid-state manufacturing techniques to be considered, with the latter providing an additional advantage by using solid materials rather than the powders used in the other techniques.

The advantages of using a functionally graded material, is that the properties can be tailored both in the axial as well as in the radial direction, simultaneously as well as separately (Figure 33). This provides a variety of engineered design options for fuel developers. No existing PM methods were found during a literatures search; therefore, a new approach was designed as part of this project. That new approach, which will be the first invention to manufacture *radially gradient* systems via PM routes, is simple, cost-effective, versatile, and straightforward [35].

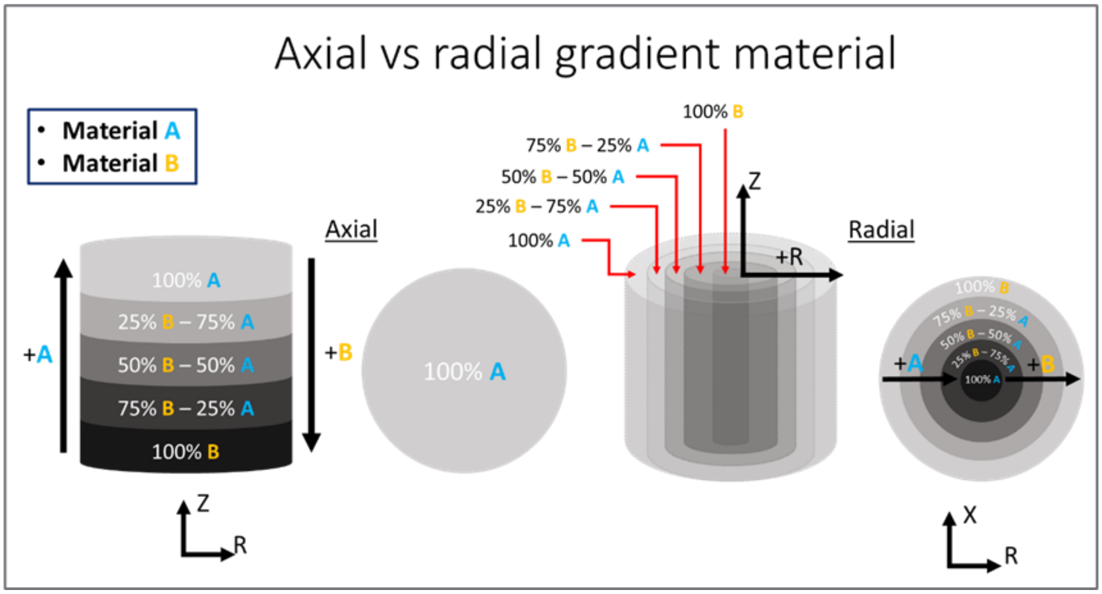

Figure 33. Differences between axial and radial gradient material using a gradient of 25% changes as an example

To date, three benchtop experiments were completed as a proof-of-concept of the newly invented loading mechanism to enable the radial gradient design. Silica sand particles were used instead of metal alloy powders to 1) minimize wasting of hazardous materials and 2) to make the process cost-effective. The silica sand particles (Hygloss) we chose were between 100 and 500 μm. Although larger than powder sizes used in AM, the chosen particles more closely resemble the size range of metal alloy powders that are typically used for HIP and other PM processes. The first benchtop experiment and the loading mechanism were described in [3] and have demonstrated the powder-loading mechanism in 1) with two gradients and 2) with three gradients using the same dividers. However, the third experiment was performed within a more prototypic simulation of the HIP can dimensions focusing on the height. The outer diameter of the can that we intend to use for the final HIP experiment is ~1.5 inches; therefore, we performed a benchtop experiment to validate the proposed powder loading mechanism using a glass beaker with nearly identical dimensions (outer diameter of ~1.67 inches). To be consistent with our previous benchtop experiments, the silica sand particles procured from Hygloss in the size range of 100–500 μm were used for this study. The design considerations for the circular dividers were 1) to ensure perfect placements inside the 50 mL glass beaker/HIP can and 2) to facilitate easy loading of the powders for both the current benchtop experiment and the future HIP experiments. The height of these dividers is designed considering the dimensions of the HIP can that we plan to use for the final experiment. The height of the HIP can is ~3 inches; thus, the designed dividers are kept above 4 inches for easy removal after loading the powders. Results of the three benchtop experiments are shown in Figure 34.

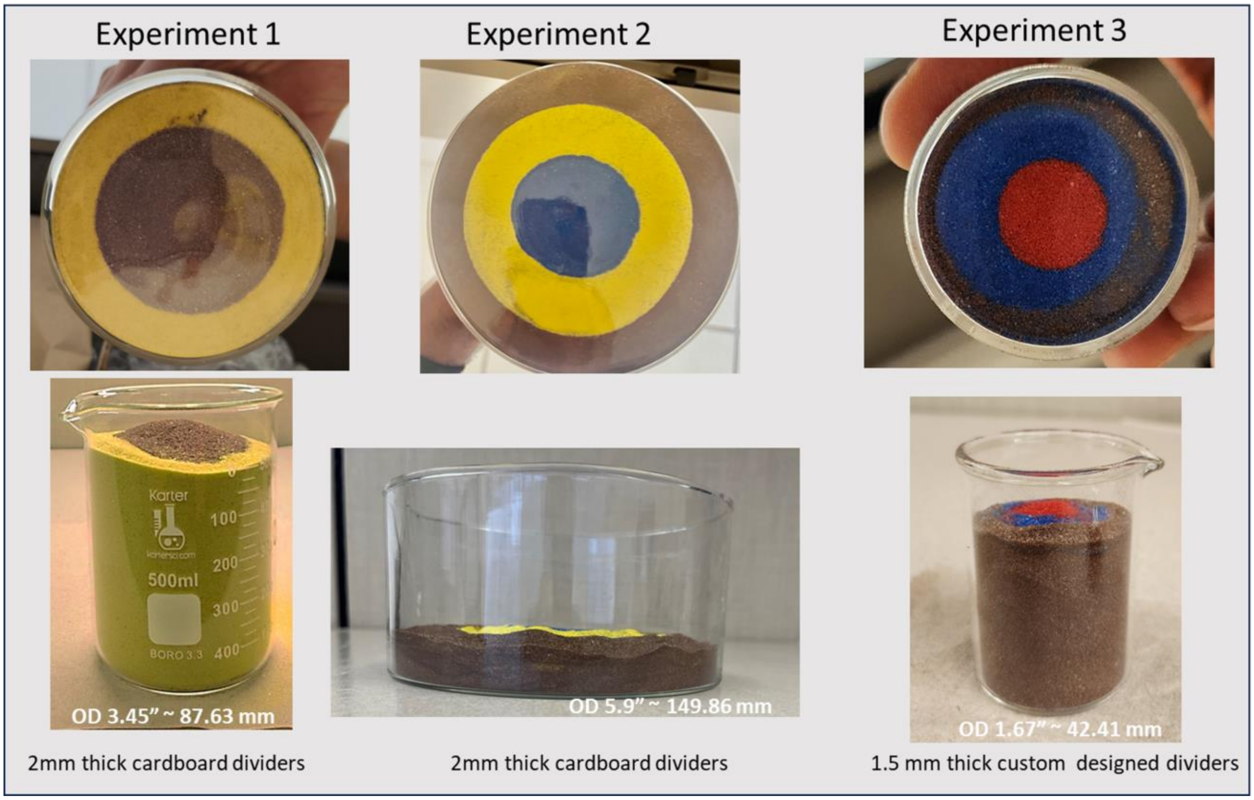

Figure 34. Results of the three powder loading benchtop experiments

4.0 Phase 4: Alloy Development and Fabrication enabled through FSAM and other Processes

Solid-phase AM is an emerging technology to produce additive manufactured parts featuring a recrystallized, fine grain, isotropic microstructure circumventing melting and solidification of the deposited material. FSLD is currently the most suitable solid phase additive manufacturing process to produce builds of high plasticizing temperature materials since it does not require expensive tooling to deposit the layers. Further information on the Friction Surfacing process can be found in [36,37]. The application of Friction Surfacing on additive manufacturing (i.e., Friction Surfacing Layer Deposition are described in [38-40].

As bases for new material developments and alloy designs, FSAM and FSLD can be used to create new materials because of the unique microstructures and solid-phase reactivities that can be achieved. Additionally, those process could be used to create new input materials for ShAPE tube forming processes. This will simultaneously enable unique materials to be available for tube forming processes, as well as possible other bulk forming materials. This will put us in a better position to continue with alloy development activities later in 2024,

4.1 FSLD Experimental Procedure, Materials and Equipment

Based on an abridged literature review, there are no published studies in the available literature on friction surfacing layer deposition of HEA. Hence, considering the resources available for this task, a simplified process parameter optimization procedure was devised to accelerate the definition of satisfactory deposition parameters for $NiCoFeCrCu_{0.12}$ (see Figure 35):

Initial process parameters were based on values reported in the literature [41,42] for comparable materials processed by SPP (e.g., friction welding).

Based on these start parameters, the rotational speed was progressively increased by constant axial force until the onset of plasticization was reached. This will define the so-called “ramp” parameters (i.e., parameters to be employed before the translation motion is started).

Once plasticization has been achieved, the translatory movement will be activated at low deposition speeds and constant axial force and rotational speed.

Deposition speed will be manually adjusted until a stable deposition process is realized.

To reach a reliable and stable deposition process, further adjustments on deposition and rotational speed might be conducted.

Once a process parameter set has been established, successive layers have been deposited on top of each other.

This procedure proved to be successful in producing acceptable depositions and allowed realization of two builds. However, this is the first step in determining the optimum process parameter window for this HEA and allow the initial definition of the effect of process parameters on the geometrical features of the deposited layers (i.e., height and width) and on surface appearance. Details of the process parameters employed in this project are presented in Section 4.2**.**

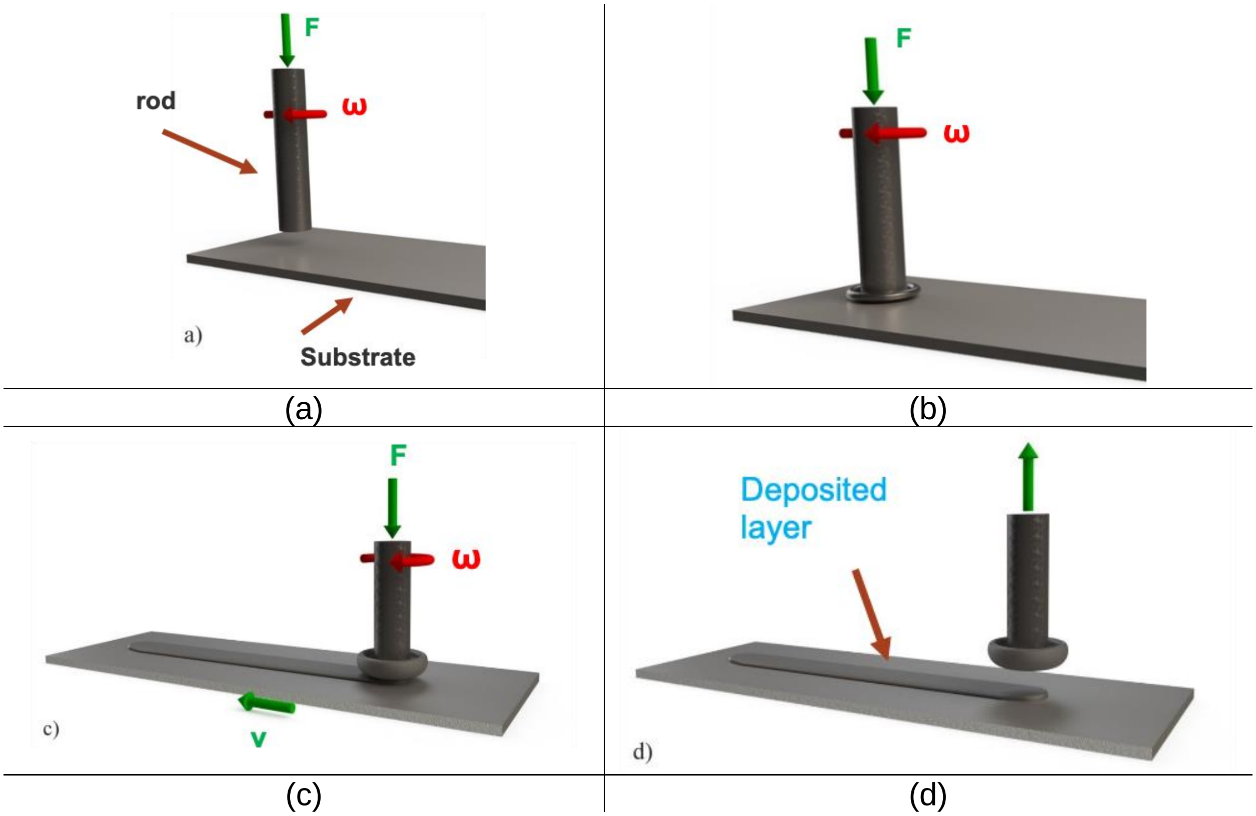

(a) (b)

(c) (d)

Figure 35. Simplified process parameters optimization procedure. (a) Start of the process parameter development phase: rod under an applied force F is pushed against the substrate with a pre-selected rotational speed. (b) Plasticization of the rod material, establishing plasticization parameters. (c) Once plasticization has been achieved, the translation movement of the rod starts. (d) Complete deposition of the first layer.

Consumable rods of cast and homogenized NiCoFeCrCu$_{0.12}$ HEA (i.e., 25.4 mm in diameter and 152.4 mm in length) were machined from the cast billets (Figure 36(a)). A 12.7 mm thick, 152.4 mm wide and 304.8 mm long 304 stainless steel substrate was used for this work (Figure 36(b)).

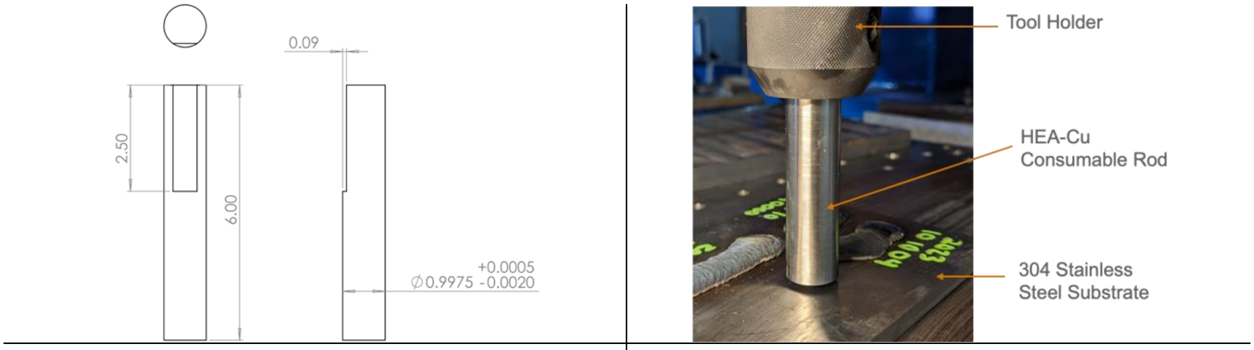

(a) (b)

Figure 36. (a) Dimensions of the consumable rod. (b) Consumable rod and substrate before deposition.

All the deposits were produced using a Transformation Technologies Inc. machine (Figure 37) with the following specification:

Maximum RPM: 1900 RPM
Maximum force: 25,000 lb (~111kN)
Maximum Torque: 500 ft-lb (670 Nm)
Maximum deposition speed: 3 m/min
X Operating Range: ~4 feet (1.2 meter)
Y Operating Range: 3.9 inches (99 mm).

The machine operates in position, force, and temperature control modes.

Figure 37. Transformation Technologies Inc. machine used to produce friction surfacing layers

To better understand the metallurgical phenomena taking place during deposition, thermal cycles have been recorded using a Fluke Infrared Imager (Figure 38). Images were recorded for each layer at a frequency of 30 Hz. Additionally, temperature measurements also were obtained from the consumable rod. For those measurements, a K-type thermocouple was embedded in the consumable rod.

Figure 38. Thermal measurements during friction surfacing layer deposition

4.2 Fabrication Results

4.2.1 Friction Surfacing Layer Deposition

Once a parameter set has been determined using the procedure described in Section 4.1, two short layers were deposited to evaluate process stability (Run 1 and Run 2). These short experiments confirmed the suitability of the selected parameter, Table 5.

The successful deposition of the first long layer (Run 3) followed. Figure 39 presents the two initial trials and the first deposited long layer. *This successful layer deposition is possibly the first ever dissimilar combination of a HEA layer deposited on a SS substrate. Such a configuration might offer opportunities to potential applications in which an HEA is used as a coating on SS parts.*

Table 6. Process parameters used for all layers deposited in this task

No.	Plunge	Rotation Rate (RPM)	Traverse Velocity (mm/min)	Forging Force (kN)
3	0.5 mm 2.5 mm/min	800	50	15

Figure 39. Two initial trials (short layers) and a long deposit

Figure 40 presents the process diagram generated by the machine controller for the long layer (Run 3). The diagram displays a very stable deposition process in which axial force and torque remained very much constant in the steady-state phase of the process. Peak forging force during plunge corresponds to the onset of shear deformation. In this case, it is 15.5 kN, which is equivalent to ~30.6 MPa. Average processing torque during steady-state deposition is 48 Nm, and power input is approximately 3.9 kW. Figure 41 shows the deposition of Run 3.

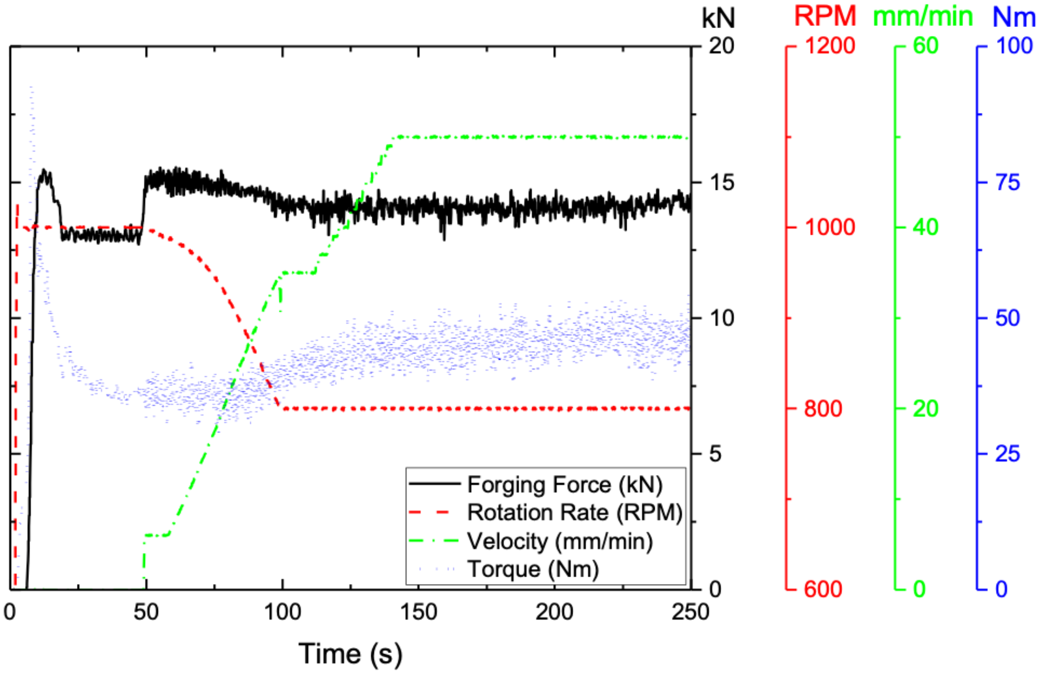

Figure 40. Process diagram for Run 3 (first long layer)

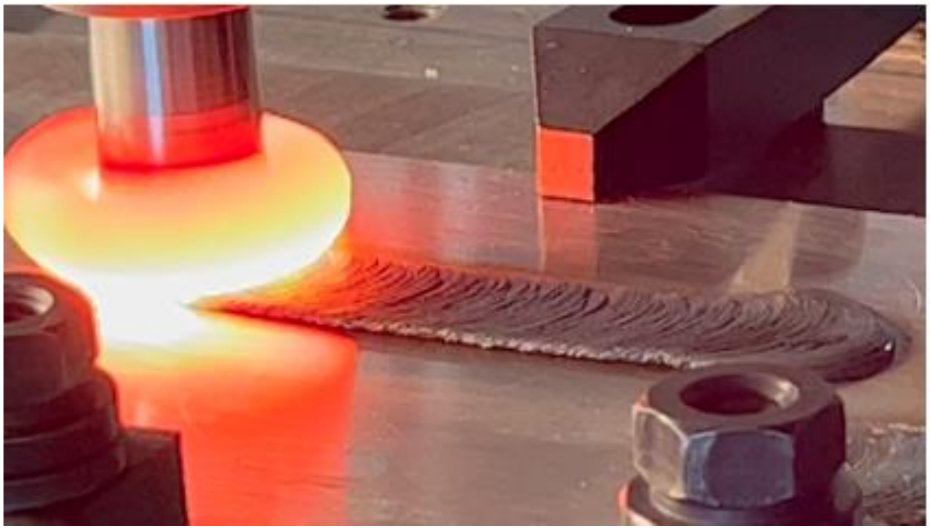

Figure 41. View of the deposition of the long layer (run 3) in the steady-state phase of the deposition

The same process parameters were used to deposit two additional layers on top of the first one. The interlayer temperature (i.e., the temperature of the previous layer before deposition of the following layers was room temperature in all cases). The surface of the layers was slightly brushed to have identical surface conditions between the layers. Figure 42 shows the three layers after deposition, and Figure 43 shows the subsequent two four-layered structures that were built.

(a) (b) (c)

Figure 42. Images of the three deposited layers: (a) first layer (Run 3), (b) second layer (Run 4), and (c) third layer (Run 5)

Figure 43. Two four layered HEA structures were fabricated successfully. The top structure was used for destructive analysis as described in section 5.3.

4.2.2 Thermal Cycle Measurements

Evaluation and analysis of the thermal data is currently in progress. This section reports the initial results compiled from the infrared camera and the thermocouple readings obtained from the consumable rod.

Figure 44 presents results obtained from measurements conducted during the deposition of Run 4 (second layer, Figure 42(b)). As it can be seen, maximum temperatures varied between approximately 850°C and 915°C in the steady-state phase of the process, the latter being the peak temperature recoded during the deposition. Temperature measurements were focused primarily on flash during deposition. The layer rapidly cools to ~380°C and remains hot until the end of the process.

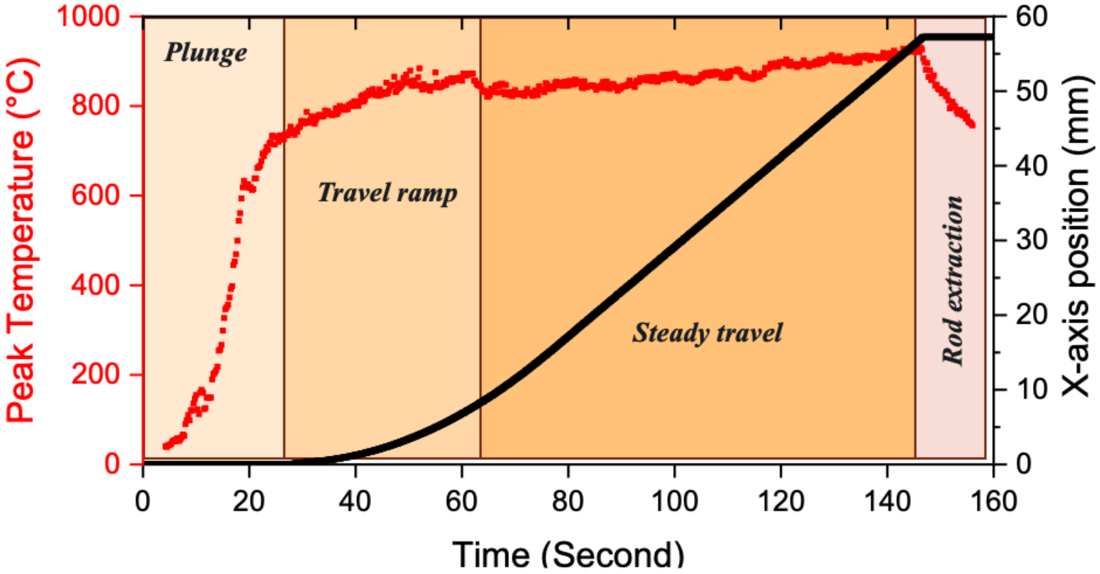

Figure 44. Results of the infrared thermal measurements. Temperature measurements were focused primarily on flash during deposition.

In Figure 45, the temperature recorded in the rod has been superimposed on the process diagram from Run 4 (second layer, Figure 42(b)). It must be noted that thermocouple was gradually pushed out of the rod as it was consumed, and the precise location of the measurements is unknown. Therefore, these results just give an indication of temperature development during deposition. The maximum temperature recorded by the embedded thermocouple is approximately 1,290°C in a region possibly close to the shear layer.

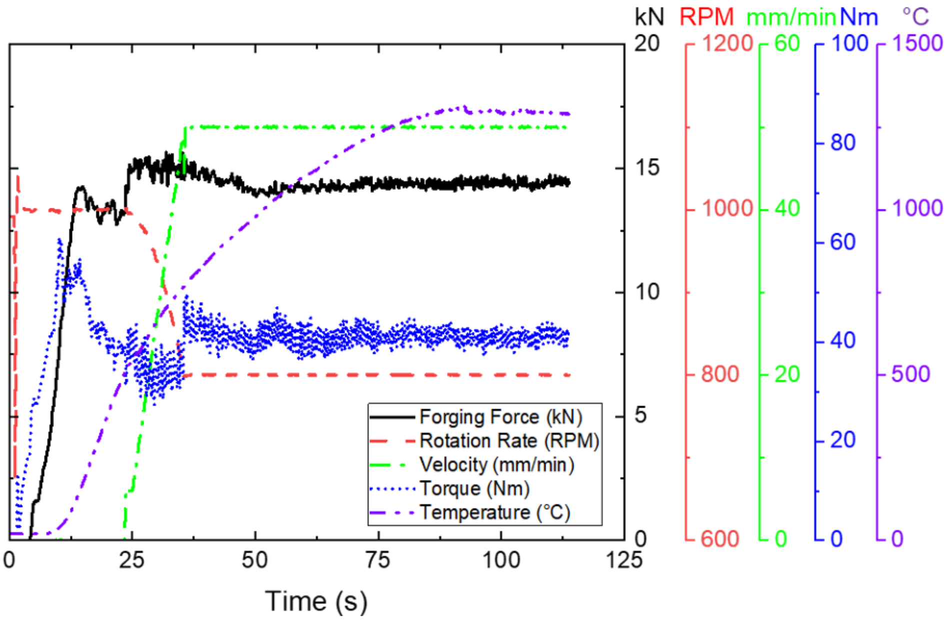

Figure 45. Temperature recorded in the rod during deposition of Run 4 (second layer). The recorded temperature has been superimposed on the process diagram from Run 4. The thermocouple has been gradually pushed out of the rod as it was consumed, and the precise location of the measurements is unknown.

4.3 Test and Analysis

Test and analysis samples have been prepared from the four-layer build as shown in Figure 46. Details of sample preparation, equipment and procedures of the microstructural analysis and hardness testing are presented elsewhere in this report.

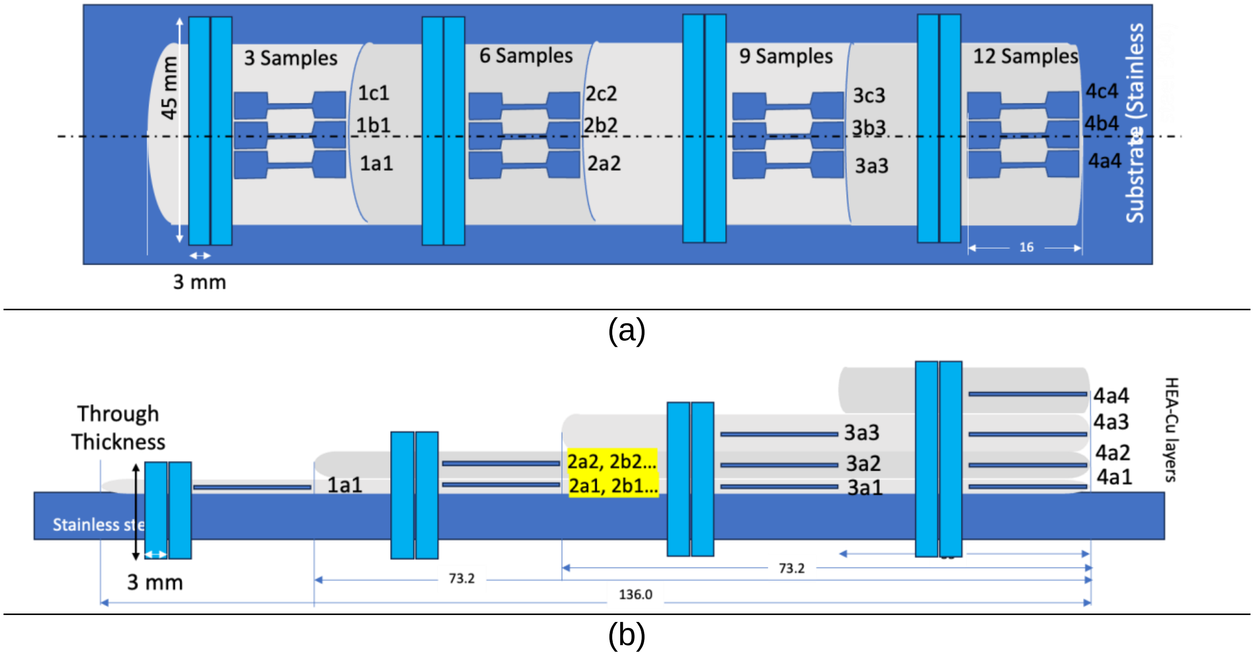

Figure 46. Cutting plan for the four-layer build, including samples for microhardness and microstructure analysis for each layer, 12x mini-tensile samples for layer 1, 9x mini-tensile samples for layer 2, 6x mini-tensile samples for layer 3 and 3x mini-tensile samples for layer 4

4.3.1 Mini-Tensile Testing

Mini-tensile samples Figure 47 were used to determine the mechanical properties of the individual layers in the build (sample extraction locations in Figure 46. The evaluation and analysis of the tensile testing results is currently in progress. This section reports the initial results obtained from the testing. These results are currently being correlated to the location of the sample and the respective thermal history to have a meaningful analysis of the results. The failure modes are also being presently assessed. Table 7 presents the obtained results.

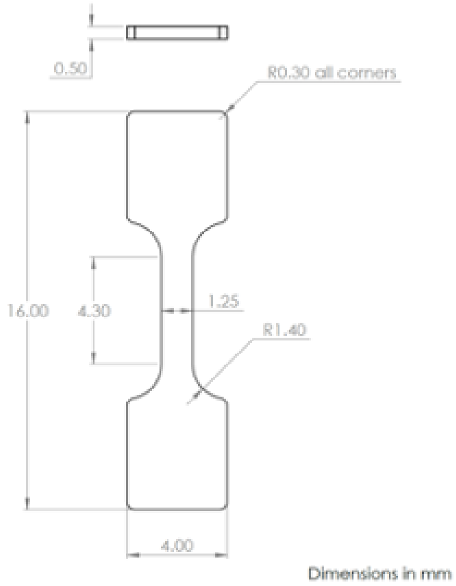

Figure 47. Dimension of the mini-tensile sample

Table 7. Tensile testing results (mini-tensile samples)

Specimen label	Width [mm]	Thickness [mm]	Maximum Load [N]	Maximum Stress [MPa]
1a1	1.28	0.52	375.91	564.8
1b1	1.28	0.50	365.13	570.5
1c1	1.28	0.51	373.61	572.3
2a1	1.31	0.51	372.21	557.1
2a2	1.30	0.50	371.75	571.9
2b1	1.29	0.50	381.31	591.2
2b2	1.28	0.75	524.94	546.8
2b2	1.28	0.75	636.40	662.9
2c1	1.29	0.50	375.43	582.1
2c2	1.28	0.78	673.88	675.0
3a1	1.29	0.51	392.31	596.3

4.3.2 Microstructural Characterization

Figure 48 shows the montage of SEM images where the layer thickness and various interfaces are visible. The approximate layer thickness for first, second, third, and fourth layers are 2.5 mm, 2.3 mm, 1.9 mm, and 1.2 mm respectively. The interface between the 316 stainless steel substrate and first deposited layer shows a fully bonded joint between the two dissimilar materials. The interfaces between different layers are approximately 1 mm in width and require higher resolution analysis for phase identification. The interface regions seem to have smaller grains with many of dark particles which might be broken remnants from superficial oxide layers present on the previous deposition.

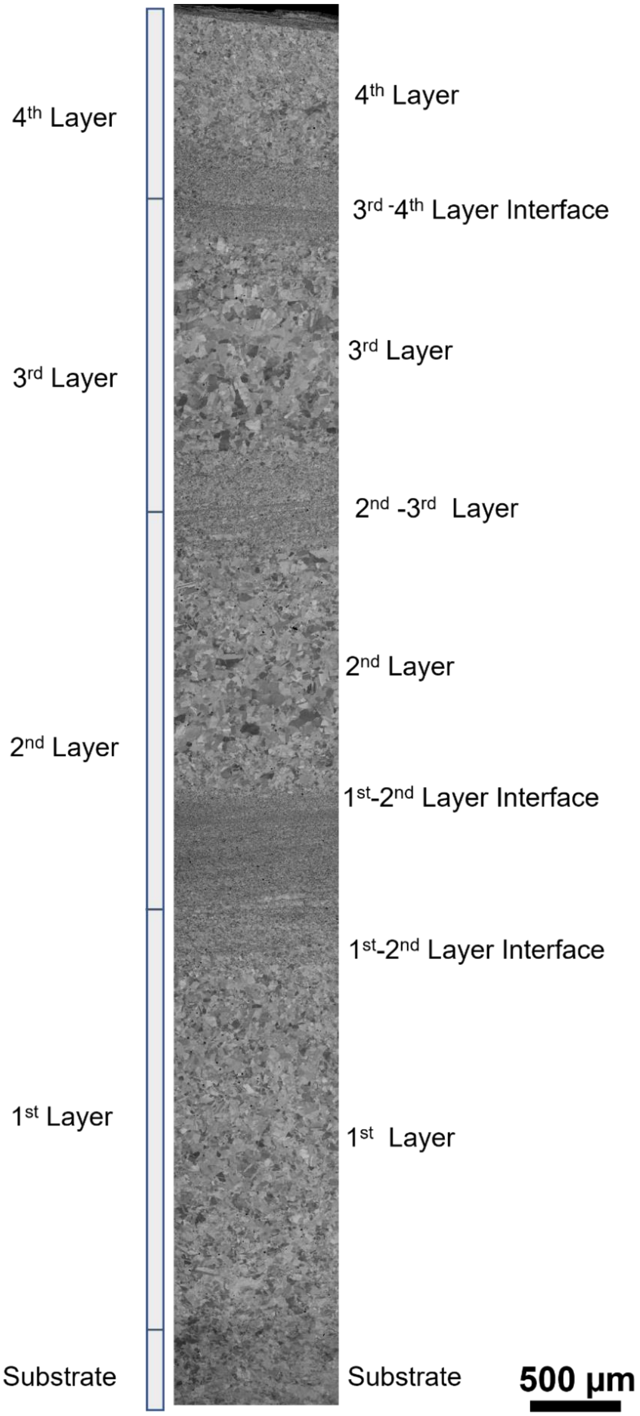

Figure 48. Montage of SEM images that shows four layers of depositions and interface regions from the traverse section of the Cu-HEA.

Figure 49 shows SEM images of layers and layer interfaces with multiple magnifications for better visualization of microstructure. The grain sizes near the interfaces are smaller as compared to central part of layers. These grain size differences are mostly due to the re-heating of layer surface when the next layer is deposited. The highest magnification images clearly show the distribution of dark particles at the interfaces.

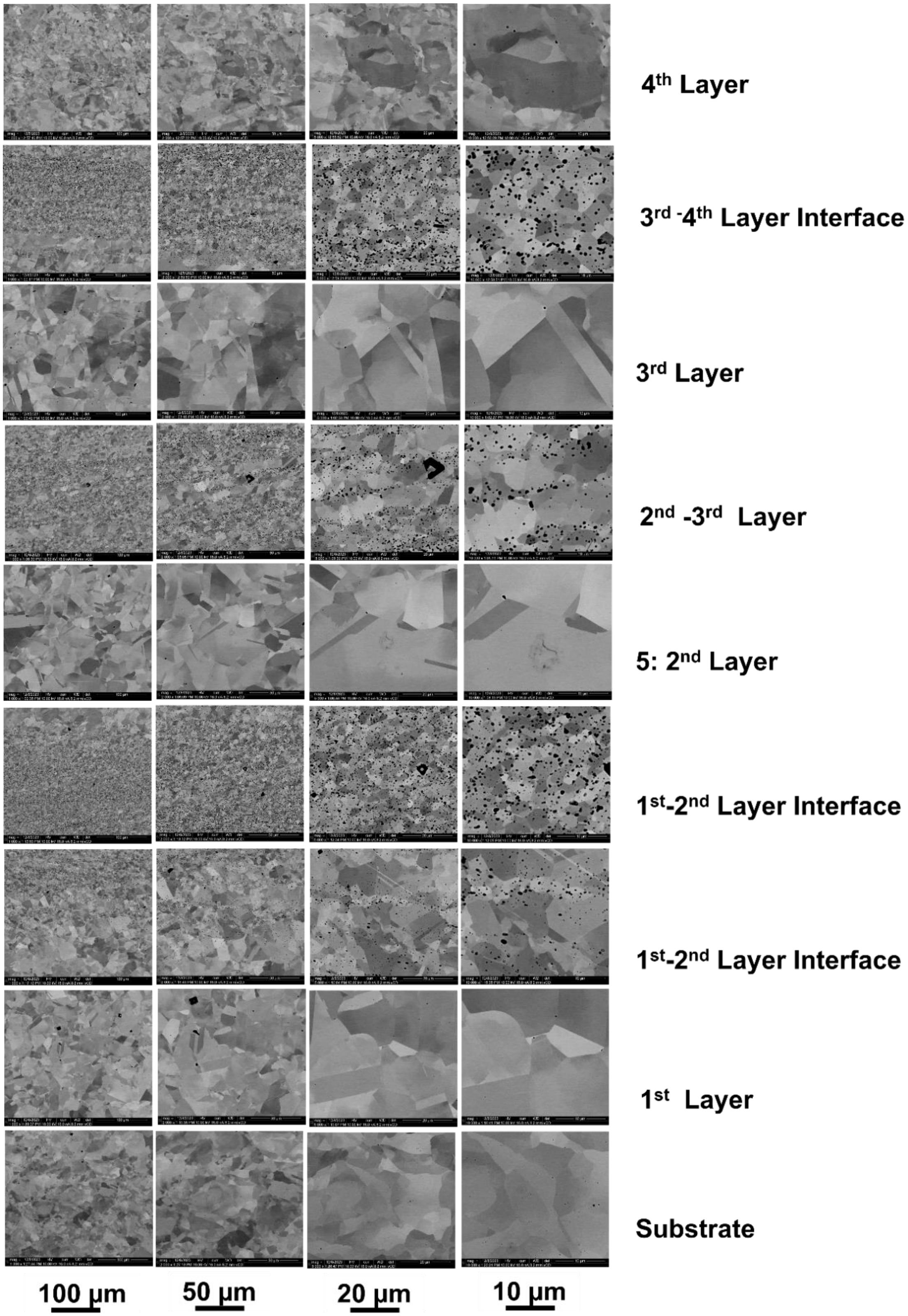

Figure 49. Series of SEM images with different magnifications across the four layers of deposition in FSLD process of Cu-HEA

Figure 50(a) shows a SEM image with all four layers of deposition and the areas where EBSD analysis were carried out are marked by yellow boxes. The de-bonded regions of layers, present at both ends, are clearly visible. These debonding are usually due to the less or absence of pressure from the tool head and they are machined out for a dense final product. Figure 50(b) shows the IPF maps from all four layers and the interface between the second and third layers. The IPF shows the presence of an FCC matrix with no sign of Cu-precipitates. The grains in this transverse view are nearly equiaxed. The top of the fourth layer seems to have extensive porosity.

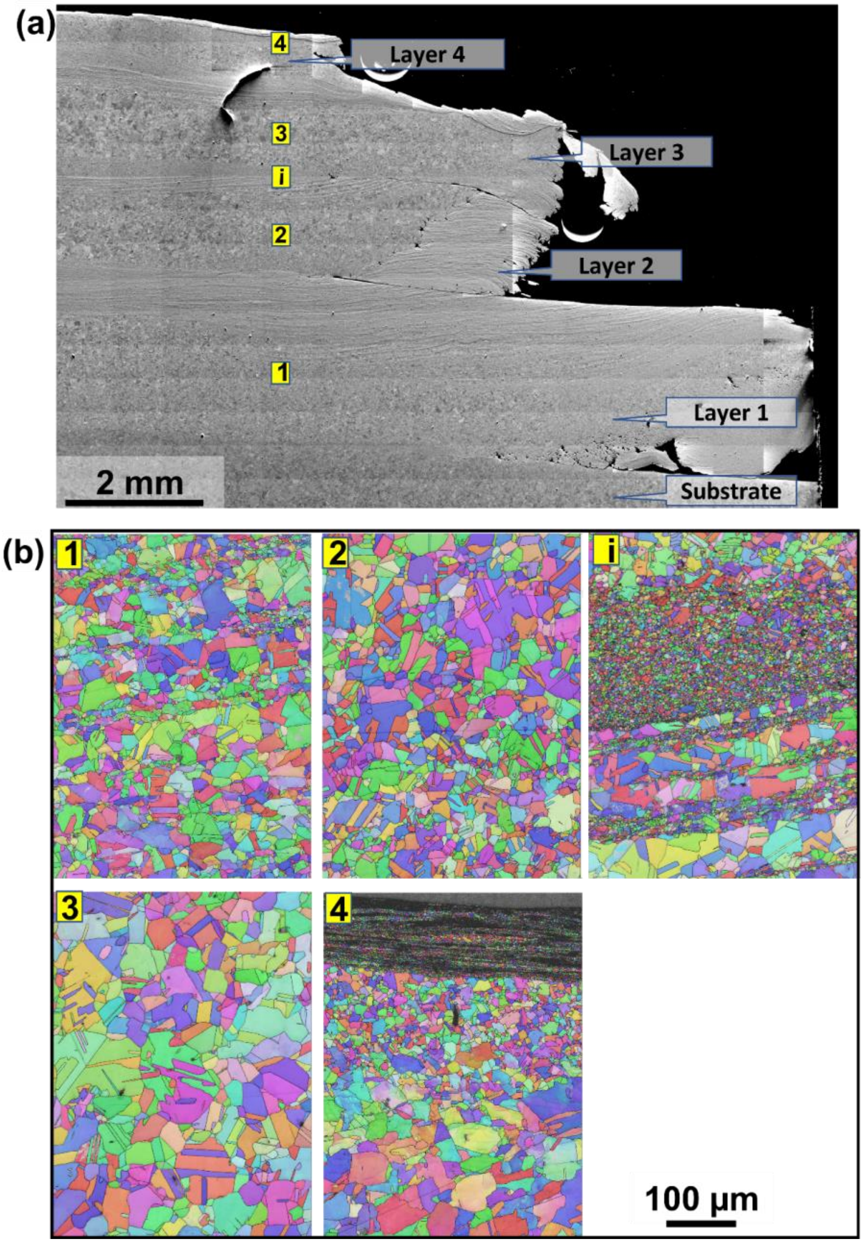

Figure 50. (a) SEM images of FSLD processed Cu-HEA marked by the spots for EBSD mapping. (b) EBSD maps from different layers and interfaces.

The grain size of these regions was determined and are presented in Figure 51 and Table 8. The grain sizes in the bulk of the layers are in the range of 20-30 µm, while the interface has smaller grains with average value of 12 µm. The extent of grain refinement in the FSLD process appears to be smaller as compared to that in ShAPE process in the same alloy. However, the grain refinement is quite significant when compared to that in as-cast and homogenized sample.

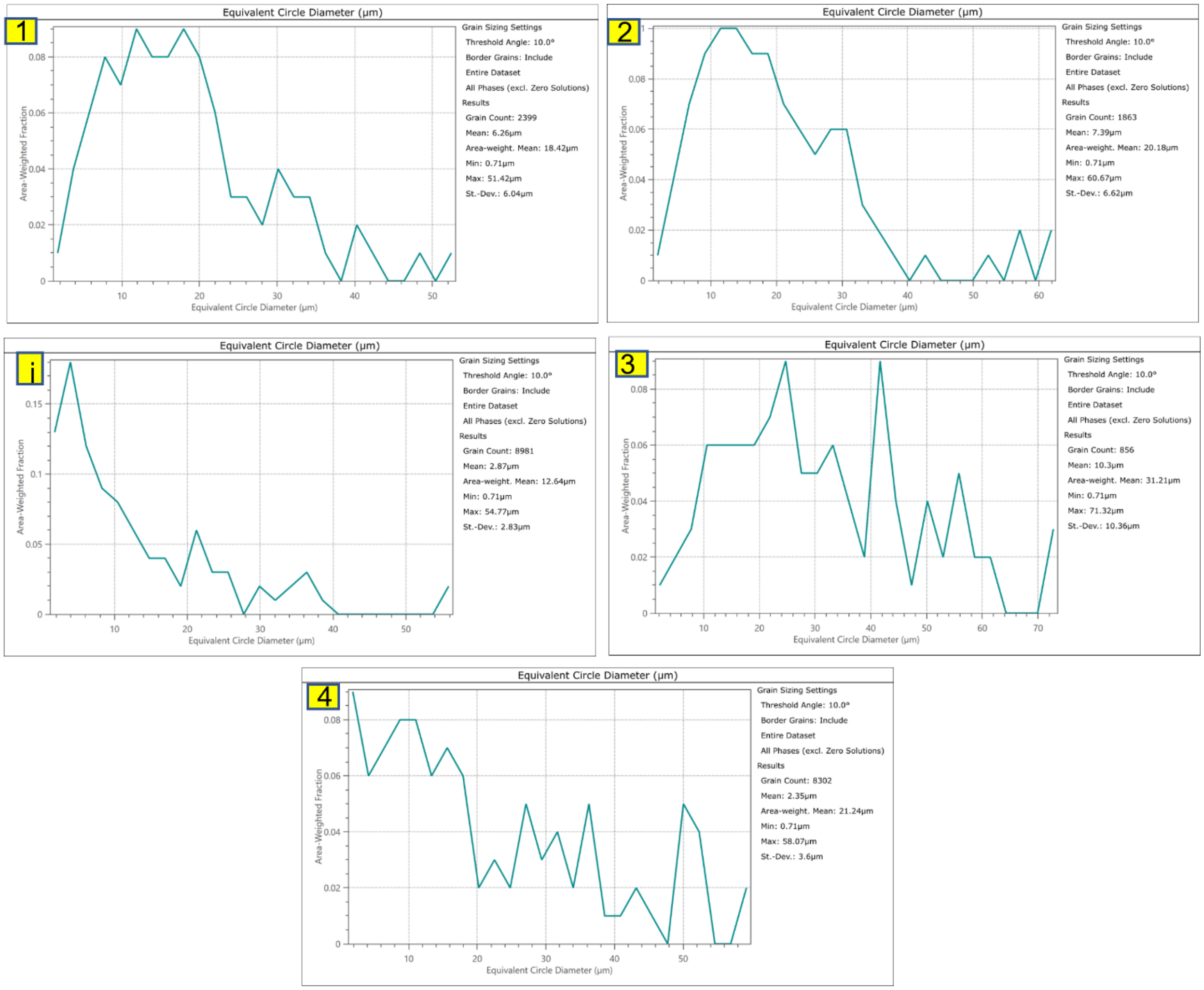

1

Grain Sizing Settings
Threshold Angle: 10.0°
Border Grains: Include
Entire Dataset
All Phases (excl. Zero Solutions)
Results
Grain Count: 2399
Mean: 6.26µm
Area-weight. Mean: 18.42µm
Min: 0.71µm
Max: 51.42µm
St.-Dev.: 6.04µm

2

Grain Sizing Settings
Threshold Angle: 10.0°
Border Grains: Include
Entire Dataset
All Phases (excl. Zero Solutions)
Results
Grain Count: 1863
Mean: 7.39µm
Area-weight. Mean: 20.18µm
Min: 0.71µm
Max: 60.67µm
St.-Dev.: 6.62µm

i

Grain Sizing Settings
Threshold Angle: 10.0°
Border Grains: Include
Entire Dataset
All Phases (excl. Zero Solutions)
Results
Grain Count: 8981
Mean: 2.87µm
Area-weight. Mean: 12.64µm
Min: 0.71µm
Max: 54.77µm
St.-Dev.: 2.83µm

3

Grain Sizing Settings
Threshold Angle: 10.0°
Border Grains: Include
Entire Dataset
All Phases (excl. Zero Solutions)
Results
Grain Count: 856
Mean: 10.3µm
Area-weight. Mean: 31.21µm
Min: 0.71µm
Max: 71.32µm
St.-Dev.: 10.36µm

4

Grain Sizing Settings
Threshold Angle: 10.0°
Border Grains: Include
Entire Dataset
All Phases (excl. Zero Solutions)
Results
Grain Count: 8302
Mean: 2.35µm
Area-weight. Mean: 21.24µm
Min: 0.71µm
Max: 58.07µm
St.-Dev.: 3.6µm

Figure 51. Compilation of plots of grain size distributions in different regions in the FSLD processed Cu-HEA

Table 8. Change in grain sizes across the length of the Cu-HEA sample after FSLD

Sample	Grain Size (µm)
Layer 1	18.42 ±6.04
Layer 2	20.2 ±6.62
Layer 2-3 Interface	12.64 ±2.83
Layer 3	31.21 ±10.36
Layer 4	21.24 ±3.6

4.3.3 Hardness Measurements

Figure 52(a) shows an optical image of the FSLD layers of Cu-HEA with indent locations for hardness measurement along both vertical and horizontal directions. Hardness was measured in horizontal direction along each layer, and they are named as L-1, L-2, L-3 and L-4 for Layer-1, Layer-2, Layer-3 and Layer 4, respectively. Additionally, hardness was measured in three different locations along vertical direction from the substrate to the top of L-4, which covers areas in all four layers and their interfaces. These three locations are named IL-1, IL-2, and IL-3.

Figure 52(b) is a plot of the hardness values taken from individual deposited layers. It should be noted that the hardness from the extreme ends of the material where layer de-bonding occurs can be disregarded. It appears that the hardness slightly increases from left to right in this transverse section of the sample for each layer when the data points are considered from the central parts of the layers. This marginal increase in hardness from left to right most probably is due to changes in grain size. Further studies of grain sizes from different sections can confirm this finding.

Figure 52(c) shows the plot of hardness values taken along vertical directions at three different regions. It can be observed that the hardness periodically varies along top to bottom direction as the measurements include data points from different layer interfaces. Increases in hardness in regions near layer interfaces are due to significantly lower grain sizes at those locations. The average value of hardness in each layer is provided in Table 9, which indicates that there is no significant difference in hardness value of individual layers.

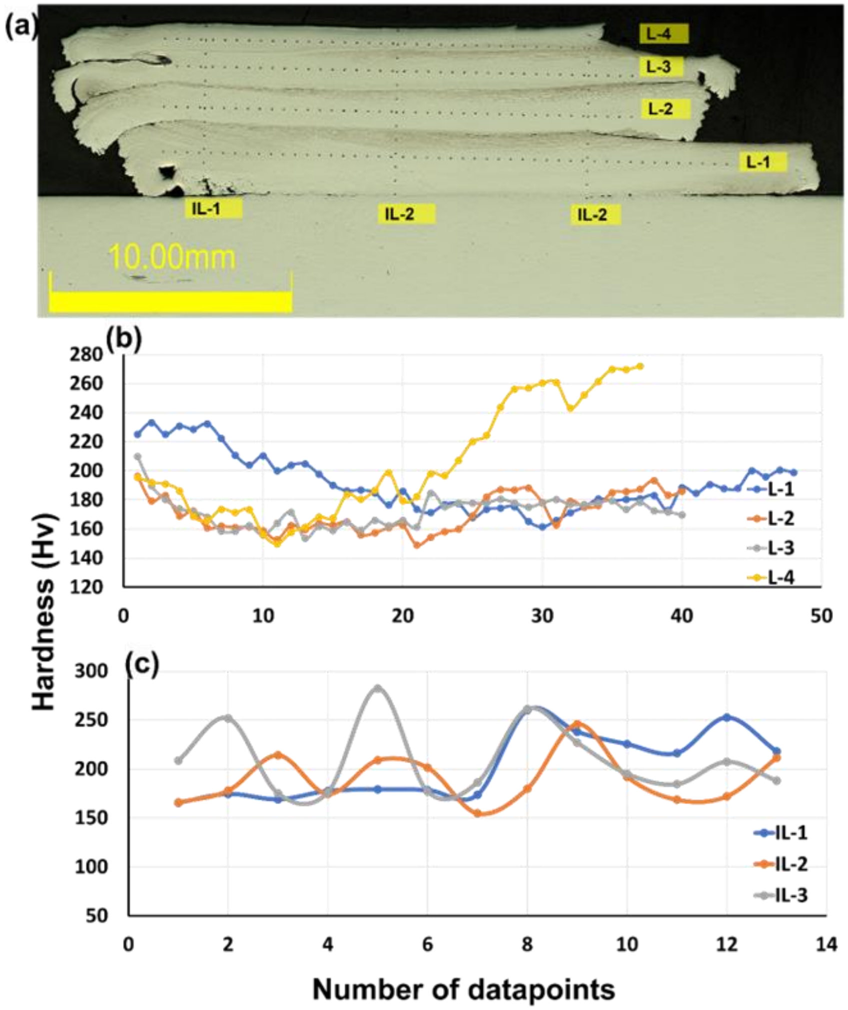

Figure 52. (a) Optical image of the FSLD-processed Cu-HEA and indents for hardness measurements along vertical and horizontal lines. (b) Hardness value plot in the four deposition layers along the horizontal line (from left to right). (c) Hardness value plot in the three vertical directions that encompass four layers and interfaces along the vertical line (from top to bottom).

Table 9. Changes in average hardness value across the length of the Cu-HEA sample after FSLD processing

Sample	Average Hardness (HV)
FSLD- Layer 1	185.3
Layer 2	169.6
Layer 3	170.1
Layer 4	172.2

5.0 Summary

The Cu-HEA was processed by two solid state processing routes namely ShAPE and FSLD. This section summarizes the findings of the post-processing characterization.

5.1 ShAPE

1. An attempt on producing a hollow tube of Cu-HEA was successful for the first time. While the tube length was nearly 2.5-inch, and some of the extrusion materials (IN718) was found to be fused with HEA-tube, further process parameter optimization is needed for producing longer tube structure of HEAs without fusing with tooling materials.
2. The electron microscopy image clearly shows the combined effects of elevated temperatures and mechanical deformations on the refinement of grain sizes. The starting materials (as cast and homogenized materials) had an average grain size of 660 µm. But the ShAPE processing was able to refine the grain structure significantly to produce grain size of 5-7 µm. This method of extreme refinement of grain can enhance the grain boundary strengthening in HEAs. The mid-section of the tube seems to have marginally finer grains compared to that in both ends of the tube.
3. The hardness in ShAPE-processed Cu-HEA also was improved to an average HV value of 185 as compared to that of cast material (HV = 115). The average hardness for start, middle and end sections were 178, 186, and 186 HV, respectively in the longitudinal direction. Also, the average hardness for start, middle, and end sections were 173, 203, and 185 HV, respectively in the transverse direction. This enhancement of hardness is most probably due to grain boundary strengthening.
4. It can be speculated from the moderate improvement of hardness value in the ShAPE processed sample that the Cu-HEA in this process condition does not contain Cu-rich precipitates. Otherwise, there would have been a significant increase in hardness value in the extruded HEA tube.

5.2 FSLD

1. The fabrication of higher volume in the build direction was successful for Cu-HEA by FSLD where four layers of Cu-HEA alloy were deposited.
2. This is the first reported successful deposition of a Cu-HEA with the FSLD technology. The fully bonded interface between the 316 SS substrate and first deposited layer as well as subsequent layers were good. The interface regions showed finer grain structures and dark particles that might be broken remnants from superficial oxide layers present on the previous deposition. This is possibly due to combined effects of thermo-mechanical stresses and a heat affected zone due to a new top layer deposition.
3. The successful deposition of the Cu-HEA on 316 SS also has demonstrated that the FSLD process can successfully produce dissimilar materials (i.e., functionalized, builds). This results clearly shows that FSLD is both an effective AM technology and a scalable HEA cladding manufacturing route.
4. The intense material deformation and flow under the tool head can influence the deposited layer thickness. Further optimization of the process parameter is needed for uniform layer deposition of HEAs.

5. The electron microscopy image clearly shows the combined effects of elevated temperatures and mechanical deformations on the refinement of grain sizes in this solid-state processing. In this process, the grain size appears to change along the build direction, particularly in the layer interface regions where finer grains of nearly 12 µm were observed as compared to that in the centers of the layers where it was in the range of 20–30 µm.
6. The extent of grain refinement in the FSLD process appears to be smaller as compared to that in ShAPE process in the same alloy.
7. The SEM images do not show the formation of Cu precipitates in the alloy in this set of processing condition.
8. The hardness in FSLD processed Cu-HEA was found be to improve as compared to that in the as-cast samples mostly due to grain refinement in this solid-state processing. Furthermore, the hardness of the first layer of the FSLD processed Cu-HEA appears to be marginally higher (185 HV) than the other layers such as second layer (170 HV), third layer (170 HV) and fourth layer (172 HV) could also be attributed to the grain refinement.
9. The grain sizes and the corresponding hardness value appear to periodically change across the build direction of the FSLD Cu-HEA.
10. The average tensile strength of the FSLD processed Cu-HEA is ~590 MPa, which is significantly higher that the base NiCoCrFe HEA (without Cu). The base NiCoCrFe HEA with a single-phase FCC microstructure exhibits a tensile strength of ~408 MPa [43], and thus, the significant difference in the tensile strength values observed suggest the presence of Cu- rich nano precipitates in the FSLD processed Cu-HEA. However, this needs to be validated via transmission electron microscopy analysis.

5.3 Presentations and Journal Articles

1. Li L., M. Nartu, M. Komarasamy, A. Soulami, and I. van Rooyen. "Modeling and analysis of the extreme process conditions during the fabrication of high-entropy alloys by Shear Assisted Processing and Extrusion (ShAPE)." TMS 2024, Orlando, Florida, 03/04/2024.
2. Li L., M. Nartu, M. Komarasamy, A. Soulami, and I. van Rooyen. "Modeling and analysis of the extreme process conditions during the fabrication of high-entropy alloys by Shear Assisted Processing and Extrusion (ShAPE)." Journal TBD.
3. Subhashish Meher, Mohan SKKY Nartu, Jorge F dos Santos, Isabella van Rooyen, Additive Friction Stir Deposition of High Entropy Alloys for Nuclear Applications, 10th International Conference on Advances in Materials, Manufacturing & Repair for Power Plants, October 15-18, 2024, Bonita Springs, Florida.

5.4 Outlook

The future planned work includes:

1. Mechanical properties of the as-cast and subsequently heat-treated rod
2. As a part of the ShAPE experiments, a direct extrusion setup to extrude tubes has been designed and is in the process of procurement. This setup involves materials of much higher temperature and force capabilities as was used in the very first extrusion.
3. Continuation of optimization and completion of experimental and material design tasks.
4. Future radial and axial powder HIP activities will be performed.

6.0 References

[1] Kombaiah, B., Zhou, Y., Jin, K., Manzoor, A., Poplawsky, J. D., Aguiar, J. A., Bei, H., Aidhy, D. S., Edmondson, P. D., Zhang, Y., Nanoprecipitates to Enhance Radiation Tolerance in High-Entropy Alloys. ACS Appl Mater Interfaces 2023, 15 (3), 3912-3924.

[2] S. Whalen, et.al., Manufacturing Letters, Accepted In-Press, 2023

[3] van Rooyen, I., et. al., Preliminary HEA Solid Phase Processing Development Report, PNNL-34986, September 2023

[4] Kim, Y.-K., M.-C. Kim, and K.-A. Lee, 1.45 GPa ultrastrong cryogenic strength with superior impact toughness in the in-situ nano oxide reinforced CrMnFeCoNi high-entropy alloy matrix nanocomposite manufactured by laser powder bed fusion. Journal of Materials Science & Technology, 2022. 97: p. 10-19.

[5] Ye, Y.F., et al., High-entropy alloy: challenges and prospects. Materials Today, 2016. 19(6): p. 349-362.

[6] Yao, M.J., et al., A novel, single phase, non-equiatomic FeMnNiCoCr high-entropy alloy with exceptional phase stability and tensile ductility. Scripta Materialia, 2014. 72-73: p. 5-8.

[7] Deng, Y., et al., Design of a twinning-induced plasticity high entropy alloy. Acta Materialia, 2015. 94: p. 124-133.

[8] Shi, Y., B. Yang, and P.K. Liaw Corrosion-Resistant High-Entropy Alloys: A Review. Metals, 2017. 7, DOI: 10.3390/met7020043.

[9] Ostovari Moghaddam, A., et al., High temperature oxidation resistance of W-containing high entropy alloys. Journal of Alloys and Compounds, 2022. 897: p. 162733.

[10] Pickering, E.J., et al. High-Entropy Alloys for Advanced Nuclear Applications. Entropy, 2021. 23, DOI: 10.3390/e23010098.

[11] Kumar, N.A.P.K., et al., Microstructural stability and mechanical behavior of FeNiMnCr high entropy alloy under ion irradiation. Acta Materialia, 2016. 113: p. 230-244.

[12] Zhang, Y., et al., Atomic-level heterogeneity and defect dynamics in concentrated solid-solution alloys. Current Opinion in Solid State and Materials Science, 2017. 21(5): p. 221-237.

[13] Fan, Z., et al., From suppressed void growth to significant void swelling in NiCoFeCr complex concentrated solid-solution alloy. Materialia, 2020. 9: p. 100603.

[14] Parkin, C., et al., Phase stability, mechanical properties, and ion irradiation effects in face-centered cubic CrFeMnNi compositionally complex solid-solution alloys at high temperatures. Journal of Nuclear Materials, 2022. 565: p. 153733.

[15] Kombaiah, B., et al., Phase stability of single phase Al0.12CrNiFeCo high entropy alloy upon irradiation. Materials & Design, 2018. 160: p. 1208-1216.

[16] El-Atwani, O., et al., Outstanding radiation resistance of tungsten-based high-entropy alloys. Science Advances. 5(3): p. eaav2002.

[17] S. Whalen, et. al., Journal of Manufacturing Processes, 71, pg. 699-710, 2021.

[18] Komarasamy M., et. al., Light Metals 2022, 308-313

[19] Qiu, Y., Thomas, S., Gibson, M. A., Fraser, H. L., Birbilis, N., Corrosion of high entropy alloys. npj Materials Degradation 2017, 1 (15).

[20] Hsu, Y.-J., Chiang, W.-C., Wu, J.-K., Corrosion behavior of FeCoNiCrCux high-entropy alloys in 3.5% sodium chloride solution. Materials Chemistry and Physics 2005, 92 (1), 112-117.

[21] Ralston, K. D., Birbilis, N., Effect of Grain Size on Corrosion: A Review. Corrosion 2010, 66 (7).

[22] Bohni, H., Localized Corrosion of Passive Metals. In Uhligh's Corrosion Handbook, 3rd ed.; Revie, R. W., Ed. John Wiley & Sons: Hoboken, New Jersey, 2011; pp 157-169

[23] Xie, J., Zhang, S., Dong, J., Wang, S., Wang, H., Kuang, W., Insights into the superior stress corrosion cracking resistance of FeCrAl alloy in high temperature hydrogenated water: The critical role of grain boundary oxidation. Corrosion Science 2022, 208.

[24] Lehockey, E. M., Palumbo, G., Lin, P., Brennenstuhl, A. M., On the relationship between grain boundary character distribution and intergranular corrosion. Scripta Materialia 1997, 36 (10), 1211-1218

[25] Kalsar, R., Ma, X., Darsell, J., Zhang, D., Kappagantula, K., Herling, D. R., Joshi, V. V., Microstructure evolution, enhanced aging kinetics, and mechanical properties of AA7075 alloy after friction extrusion. Materials Science & Engineering A 2022, 833, 142575

[26] Li, L., et al., “Analysis of contact conditions and microstructure evolution in shear assisted processing and extrusion using smoothed particle hydrodynamics method” Materials & Design, Volume 221, 2022

[27] Li, L., et al., “Meshfree simulation and experimental validation of extreme thermomechanical conditions in friction stir extrusion” Computational Particle Mechanics, 1-21, 2021.

[28] Yang, Tengfei, Wei Guo, Jonathan D. Poplawsky, Dongyue Li, Ling Wang, Yao Li, Wangyu Hu et al. "Structural damage and phase stability of Al0. 3CoCrFeNi high entropy alloy under high temperature ion irradiation." Acta Materialia 188 (2020): 1-15.

[29] Lu, Chenyang, Liangliang Niu, Nanjun Chen, Ke Jin, Taini Yang, Pengyuan Xiu, Yanwen Zhang et al. "Enhancing radiation tolerance by controlling defect mobility and migration pathways in multicomponent single-phase alloys." Nature communications 7, no. 1 (2016): 13564.

[30] Jin, K., C. Lu, L. M. Wang, J. Qu, W. J. Weber, Y. Zhang, and H. Bei. "Effects of compositional complexity on the ion-irradiation induced swelling and hardening in Ni-containing equiatomic alloys." Scripta Materialia 119 (2016): 65-70.

[31] Chen, Wei-Ying, Marquis A. Kirk, Naoyuki Hashimoto, Jien-Wei Yeh, Xiang Liu, and Yiren Chen. "Irradiation effects on Al0. 3CoCrFeNi and CoCrMnFeNi high-entropy alloys, and 316H stainless steel at 500° C." Journal of Nuclear Materials 539 (2020): 152324.

[32] Samal, P. and J. Newkirk, Powder metallurgy processing by hot isostatic pressing. 2015.

[33] Guillon, O., et al., Field-Assisted Sintering Technology/Spark Plasma Sintering: Mechanisms, Materials, and Technology Developments. Advanced Engineering Materials, 2014. 16(7): p. 830-849.

[34] Suárez, M., et al., Challenges and Opportunities for Spark Plasma Sintering: A Key Technology for a New Generation of Materials, in Sintering Applications, E. Burcu, Editor. 2013, IntechOpen: Rijeka. p. Ch. 13.

[35] Nartu, M., Van Rooyen, I., Yoon, D., A Novel Metal Powder Loading Mechanism for Fabrication of Radially Gradient Systems, Provisional Patent Application number: 63/539,052.

[36] Gandra, J., Krohn, H., Miranda, R.M., Vilaça, P., Quintino, L., dos Santos, J.F., Friction surfacing—A review, Journal of Materials Processing Technology, Volume 214, Issue 5, 2014, https://doi.org/10.1016/j.jmatprotec.2013.12.008.

[37] Hanke, S., dos Santos, J.F.: Comparative study of severe plastic deformation at elevated temperatures of two aluminium alloys during friction surfacing. (2017) Journal of Materials Processing Technology, 247, pp. 257-267.

[38] Shen, J., Hanke, S., Roos, A., dos Santos, J.F., Klusemann, B., Fundamental study on additive manufacturing of aluminum alloys by friction surfacing layer deposition, AIP Conference Proceedings 2113, 150015 (2019); https://doi.org/10.1063/1.5112691

[39] Rath, L., Kallien, Z., Roos, A. et al. Anisotropy and mechanical properties of dissimilar Al additive manufactured structures generated by multi-layer friction surfacing. Int J Adv Manuf Technol 125, 2091–2102 (2023). https://doi.org/10.1007/s00170-022-10685-3

[40] Zina Kallien, Lars Rath, Arne Roos, Benjamin Klusemann, Application of friction surfacing for solid state additive manufacturing of cylindrical shell structures, Additive Manufacturing Letters, Volume 8, 2024, 100184, ISSN 2772-3690, https://doi.org/10.1016/j.addlet.2023.100184.

[41] Sonar T, et al., A critical review on solid-state welding of high entropy alloys – processing, microstructural characteristics and mechanical properties of joints, Defence Technology (2023), doi: https://doi.org/10.1016/j.dt.2023.08.001. [CoCrFeNiMn and AlxCoCrFeNi alloys].

[42] Lu, Y., et al., (2022). Investigation of microstructure, texture, and mechanical properties of FeCoNiCrMn high entropy alloy during drive friction welding. Materials, Characterization, 189, 111959.

[43] Huo, Wenyi, Hui Zhou, Feng Fang, Xianjun Hu, Zonghan Xie, and Jianqing Jiang. "Strain-rate effect upon the tensile behavior of CoCrFeNi high-entropy alloys." Materials Science and Engineering: A 689 (2017): 366-369.

Appendix A – Thermal Diffusivity OF Cu-HEA

The laser flash analysis (LFA) measurements were conducted on Cu-HEA to determine the thermal diffusivity of the copper high-entropy alloy (Cu-HEA). The experiment was carried out using Netzsch LFA 457 at Idaho National Laboratory. The sample had a diameter of 12.7 mm and thickness of 1.95 mm. The samples were heated from room temperature to 1000°C with a heating rate of 3 K/min, and three individual testing were taken at each temperature. Figure 1 shows the change of thermal diffusivity with temperature for the Cu-HEA. It seems the slope changed around 700°C, which may correspond to the phase change in the alloy.

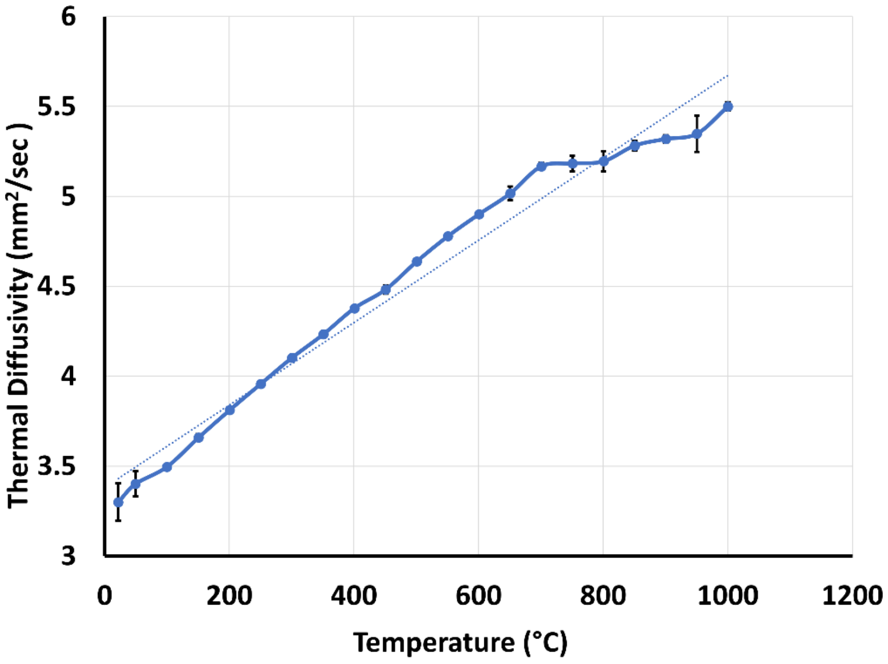

Figure A.1. Increase of thermal diffusivity in the Cu-HEA with temperature

A.1 Differential Scanning Calorimetry (DSC) Analysis of Cu-HEA

A.1.1 Calibration

Temperature and sensitivity calibrations were performed for this work. Standards of high purity with known transition temperatures were used for this calibration. Six standards were used: indium, bismuth, zinc, aluminum, silver, and gold. The system parameters were held identical to the anticipated experimental parameters and can be seen in Section 3.0. Results from the calibrations are shown in Table A.1. Using these values, temperature and sensitivity calibration curves were created for the 10 KPM heating rate. Table A.1 shows the literature data and the calibration test results for the six standards.

Table A.1. High-purity standards used for DSC calibration, and the results of onset temperature and peak area. Calibration curves were created using this data.

Standard	Sample Weight (mg)	Literature Transition Temperature (°C)	Temperature Range (°C)	Average Onset Transition Temperature (°C)	Average Peak Area (µVs/mg)
Indium	18.1	156.6	100-200	158.1	34.5
Bismuth	20.0	271.4	175-325	273.2	57.6
Zinc	14.5	419.5	375-475	420.2	100.3
Aluminum	14.8	660.3	600-710	661.3	247.0
Silver	14.1	961.8	925-1000	961.4	46.7
Gold	19.2	1064.2	1,000-1125	1062.2	23.08

A.1.2 Calibration Check

A calibration check was performed using an additional sample of high-purity zinc. Table A.2 shows the results of the calibration check.

Table A.2. Results of a calibration check using zinc

Zinc Calibration Check	
Sample wt.	13.2 mg
Literature Transition Temperature	419.5 °C
HR	10 KPM
Cycle	**Onset**
1	419.4
2	419.4
3	419.3
Average	419.36
Std. Dev.	0.058
RSD	0.014

Notes: The total average melting point of the zinc calibration check sample was **419.36**, confirming the temperature calibration was acceptable. The heat flow was within expected values; therefore, the sensitivity calibration was acceptable.

A.2 Experiment Results

A.2.1 General Parameters

The sample was evaluated in a differential scanning calorimeter DSC at a heating rate of 10 K/min. DSC parameters held constant for all samples are listed in Table A.3..

Table A.3. DSC Parameters

Parameter	Setting
Sample mass	0.1087 g
Crucible Material	Platinum with Alumina liner/spacer
Purge and Protective Gas	Argon

Purge Gas Flow Rate	20 ml/min
Protective Gas Flow Rate	50 ml/min
Furnace Atmosphere	Argon
Furnace Material	High Temperature Rh (0 to 1650 °C)
Thermocouple Type	Type S
Calibration	Temperature, Sensitivity
Heating/Cooling rate	10 K/min

Platinum sample and reference crucibles were used, with an alumina liner inside the crucibles, and an alumina spacer between the crucibles and the sample carrier. The reference and sample crucibles were placed on the sample carrier on the DSC furnace. Argon was purged through the furnace during experiments. The sample and reference crucibles were subjected to the desired temperature program, and data acquired and saved on the instrument computer. Data acquired includes information about the reference, sample crucible weight, sample weight, argon purge and protective gas flow rate, calibrations, heating rates, and temperature ranges.

Heat capacity is measured on a DSC using a multi-phase process. First, a baseline is measured using an empty crucible subjected to the same temperature program as the test sample. Second, the heat capacity of a standard, such as sapphire, is measured with the same temperature program. Third, the heat capacity of the sample is measured. Multiple runs of each phase are taken to ensure repeatability.

The heat capacity of the sample is calculated by the ratio method, with the following formula:

$$C_p = \frac{m_{standard}}{m_{sample}} * \frac{DSC_{sample} - DSC_{baseline}}{DSC_{standard} - DSC_{baseline}} * C_{p,standard}$$

where C_p is the specific heat of the sample at temperature, $C_{p,standard}$ is the specific heat of the standard (sapphire) at temperature, m is the mass of the sample or standard, and DSC is the value of the DSC signal at temperature.

A.2.2 Results

A.2.2.1 Baseline

Multiple baseline measurements were taken, to ensure repeatability, and a baseline was chosen of the multiple runs to use as the measurement baseline. Figure A.2 shows the baseline measurement using an empty sample crucible with a reference. The temperature program, the same used for the sapphire and sample measurements, heated the crucibles from 30°C to 1,000°C, at a heating rate of 10°C/min.

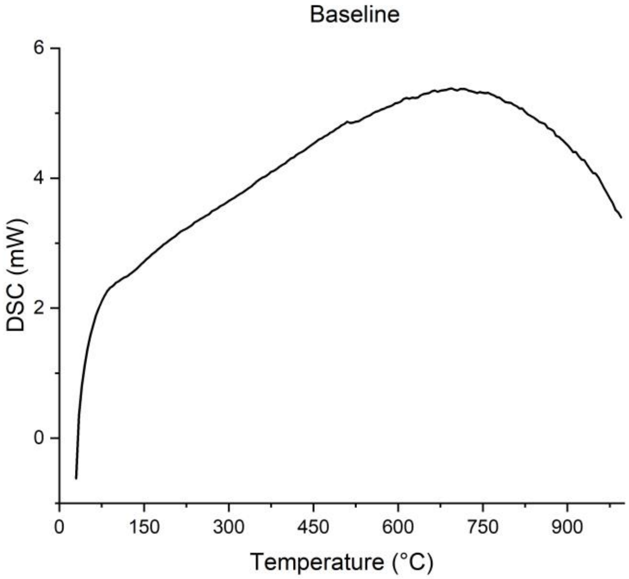

Figure A.2. Baseline for the heat capacity measurement of the HEA sample

A.2.2.2 Sapphire

Multiple sapphire runs were taken, to ensure repeatability. The final sapphire measurement was used as the standard for calculating heat capacity of the sample. The sapphire measured heat capacity was checked against literature data for sapphire, taken from the DSC Proteus Analysis software. Figure A.3 shows the heat capacity comparison for the sapphire measurement. The measured heat capacity had a maximum deviation from literature values of approximately 0.4% and was therefore deemed acceptable to use for sample analysis.

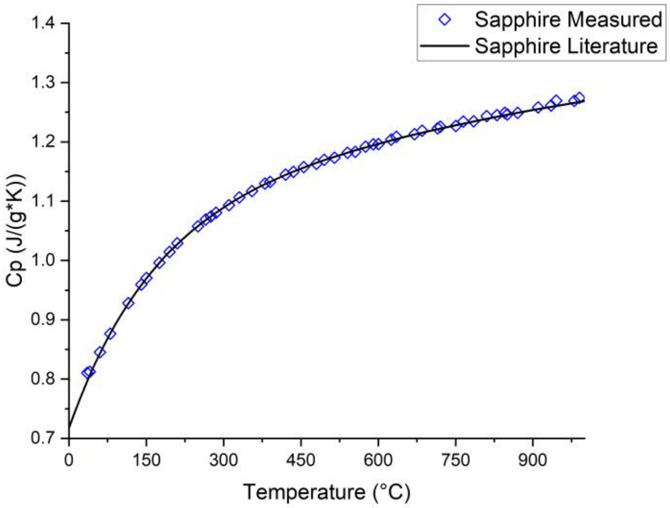

Figure A.3. Heat capacity comparison of measured and literature sapphire

A.2.2.3 Cu- HEA

Three measurement runs were taken of the sample, and an average taken of the results. The average heat capacity of the sample is reported in Table A.4. Figure A.4 shows the complete dataset, including the three individual sample runs and the average heat capacity. No mass loss was observed after measurement, and there was no change to the measurement crucible.

Table A.4. Average heat capacity of HEA Sample 1

Temperature (°C)	Heat Capacity (J/g*K)	Standard Deviation
35.8	0.537	0.0149
75.5	0.502	0.0073
115.3	0.496	0.0066
155.1	0.512	0.0055
194.9	0.522	0.0055
234.7	0.532	0.0058
274.4	0.540	0.0076
314.2	0.550	0.0086
354.0	0.559	0.0080
393.8	0.568	0.0092
433.6	0.576	0.0096
473.3	0.583	0.0105
513.1	0.588	0.0105
552.9	0.601	0.0105
592.7	0.632	0.0107
632.5	0.639	0.0105
672.2	0.637	0.0111
712.0	0.636	0.0125
751.8	0.654	0.0129
791.6	0.668	0.0132
831.4	0.669	0.0139
871.1	0.665	0.0136
910.9	0.664	0.0139
950.7	0.659	0.0182
990.5	0.665	0.0194

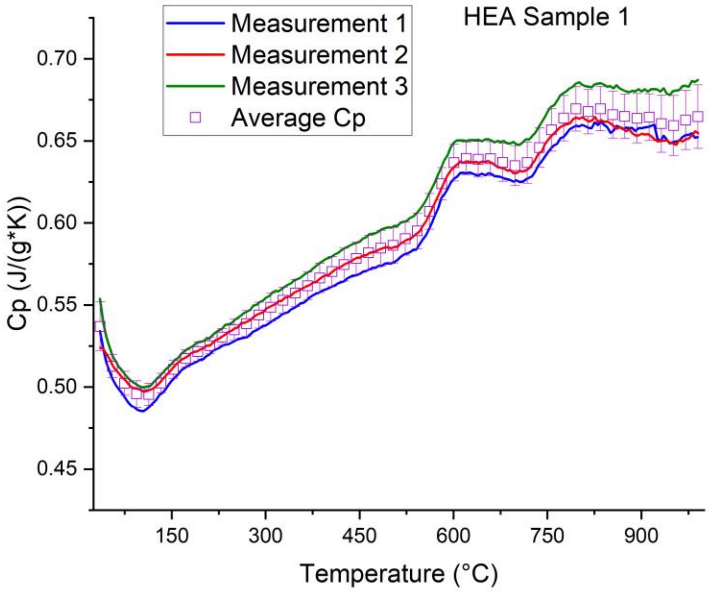

Figure A.4. Heat capacity of HEA sample 1

Pacific Northwest
National Laboratory

902 Battelle Boulevard
P.O. Box 999
Richland, WA 99354

1-888-375-PNNL (7665)

www.pnnl.gov